Multiple-relaxation-time lattice Boltzmann model for incompressible miscible flow with large viscosity ratio and high Péclet number

Xuhui Meng and Zhaoli Guo*

State Key Laboratory of Coal Combustion, Huazhong University of Science and Technology, Wuhan 430074, China

(Received 10 June 2015; published 16 October 2015)

A lattice Boltzmann model with a multiple-relaxation-time (MRT) collision operator is proposed for incompressible miscible flow with a large viscosity ratio as well as a high Péclet number in this paper. The equilibria in the present model are motivated by the lattice kinetic scheme previously developed by Inamuro *et al.* [Philos. Trans. R. Soc. London, Ser. A **360**, 477 (2002)]. The fluid viscosity and diffusion coefficient depend on both the corresponding relaxation times and additional adjustable parameters in this model. As a result, the corresponding relaxation times can be adjusted in proper ranges to enhance the performance of the model. Numerical validations of the Poiseuille flow and a diffusion-reaction problem demonstrate that the proposed model has second-order accuracy in space. Thereafter, the model is used to simulate flow through a porous medium, and the results show that the proposed model has the advantage to obtain a viscosity-independent permeability, which makes it a robust method for simulating flow in porous media. Finally, a set of simulations are conducted on the viscous miscible displacement between two parallel plates. The results reveal that the present model can be used to simulate, to a high level of accuracy, flows with large viscosity ratios and/or high Péclet numbers. Moreover, the present model is shown to provide superior stability in the limit of high kinematic viscosity. In summary, the numerical results indicate that the present lattice Boltzmann model is an ideal numerical tool for simulating flow with a large viscosity ratio and/or a high Péclet number.

DOI: 10.1103/PhysRevE.92.043305 PACS number(s): 47.11.−j, 47.20.−k

I. INTRODUCTION

Incompressible miscible flow, which is generally described by the incompressible Navier-Stokes (NS) equations and the convection-diffusion equation (CDE), is frequently encountered in many industrial areas, such as secondary and tertiary oil recovery, exploration of underground water, pollution transport, and so on [1–3]. In particular, miscible flow with a large viscosity ratio and/or a high Péclet (Pe) number, such as the recovery of heavy oil or bitumen and the transport of pollution, has been attracting extensive attention in recent years [4]. In addition, advection-diffusion systems, especially situations with high Péclet numbers, are also the focus of many studies, such as, for example, the transverse diffusive transport of miscible solutes in microchannels [5–8]. Our particular interest is in studying this type of miscible flow with a large viscosity ratio and/or a high Péclet number. Considering that both the NS equations and the CDE are strongly nonlinear, various numerical methods have been developed to simulate miscible flow over the past decades [1,2,9–12]. However, it should be noted that most of the existing numerical methods have difficulties (e.g., numerical instability) in simulating miscible flow with a large viscosity ratio and a high Péclet number [9,12]. Hence, it would be advantageous to develop efficient numerical methods that are capable of handling this problem.

The lattice Boltzmann (LB) method, which is a mesoscopic numerical method based on the kinetic theory, was already employed in the study of incompressible miscible flows. The lattice Bhatnagar-Gross-Krook (LBGK) model [1,9,10] (LBGK-A) is the most widely used model for miscible flows. However, as pointed out in numerous previous studies, the numerical accuracy and stability of the LBGK model depend strongly on the relaxation time in the evolution equation [1,9,10,13]. Considering that the relaxation time in the LBGK model for the NS equations is determined by fluid viscosity, and the relaxation time for the convection-diffusion (CD) equation is determined by the diffusion coefficient, two shortcomings of this model appear. First, as the fluid viscosity or the diffusion coefficient is relatively small, the corresponding relaxation time approaches 0.5, and as a consequence the model becomes unstable numerically. Second, a large fluid viscosity means a large relaxation time, and the no-slip boundary condition cannot be ensured unless a larger lattice is used [9]. For example, for the heavy-oil recovery or the bitumen recovery problem, the viscosity of displacing fluid is always much smaller than the displaced one in practice, meaning that one of the relaxation times related to the fluid viscosity has to be taken small, while the other one is large. In addition, the diffusion coefficient is usually quite small in such problems, suggesting that the relaxation time related to the diffusion coefficient is close to 0.5. Consequently, the small relaxation time related to the viscosity and/or diffusion coefficient always leads to numerical instability, while the large relaxation time related to the viscosity causes the problem of imprecise implementation of the no-slip boundary condition. These difficulties mentioned above restrict the applications of the model in this field.

To overcome the deficiencies in the LBGK model, several efforts have been made to improve the performance of this model in recent years. For instance, Gabbanilli *et al.* [14] tried to avoid numerical instability by imposing lower and upper bounds on the fluid viscosity in non-Newtonian flow. However, this artificial treatment may introduce extra numerical errors in computations. Later, Xiang *et al.* [15] introduced another parameter β into the second-order moment condition, which can be adjusted to avoid a small relaxation time, and the numerical stability improved. However, a recent study revealed that the improvement is not significant [16]. Recently, Wang *et al.* [18]

*zlguo@hust.edu.cn

performed simulations of non-Newtonian flow with a model developed from the lattice kinetic scheme (LKS). The LKS model was first proposed by Inamuro *et al.* [17] to reduce the memory requirement for simulating incompressible flows as well as heat transfer. By adding a term related to the shear rate (or scalar gradient) into the equilibrium distribution functions, the fluid viscosity (or diffusion coefficient) of the LKS model is determined by an additional tunable parameter with a fixed relaxation time (i.e., 1.0). Consequently, there is no need to store the velocity distribution functions with this treatment, and the memory requirement decreases significantly. However, the numerical stability of this algorithm was not analyzed in their work, and the original LKS model does not conserve mass locally. Wang *et al.* improved the LKS model in order to ensure that the mass was conserved, and the relaxation time in their work is no longer fixed as 1.0 but can be adjusted in a proper range to ensure the numerical stability of the method. Most recently, Yang *et al.* [16] developed a model for the incompressible NS equations and CDE based on the LKS model (LBGK-B). As demonstrated in Refs. [16,18], both of the models developed from the LKS have improved the numerical stability in comparison with the standard LBGK model.

It should be noted that the works based on the LKS model mentioned above approximate the collision operator with a single-relaxation-time (SRT) or BGK approximation. However, as Pan *et al.* [19] pointed out, the use of SRT models may bring about some unphysical artifacts, such as the inaccurate boundary conditions (especially for situations with large relaxation times) and the viscosity-dependent permeability for porous media. On the other hand, using a multiple-relaxation-time collision model can significantly reduce this deficiency, and it can improve numerical stability further [20–23]. Recently, Zhang *et al.* [24] performed simulations of the miscible flow with the MRT model (MRT-A), and the imprecise implementation of the no-slip boundary condition was eliminated with this treatment. However, due to the fact that the relaxation times are directly determined by the viscosity and/or diffusion coefficient, numerical instability will also be encountered in this model as the viscosity and/or diffusion coefficient is rather small. Considering the merits of the multiple-relaxation-time collision model as well as the superior stability of the LKS model, in this work we will develop an MRT model (MRT-B) on the basis of the LKS model for incompressible miscible flow with a large viscosity ratio and high Pe.

The rest of the paper is organized as follows. The modified MRT model for the incompressible miscible flow is presented in Sec. II. Section III contains a series of numerical simulations that are carried out to test the performance of the model. Finally, a summary is presented in Sec. IV.

II. AN MRT MODEL BASED ON LKS FOR THE NS AND CD EQUATIONS

In this section, an MRT model for the incompressible NS and CD equations is presented. The macroscopic equations for incompressible miscible flows are as follows:

$$\nabla \cdot \boldsymbol{u} = \boldsymbol{0}, \tag{1a}$$

$$\partial_t \boldsymbol{u} + \nabla \cdot (\boldsymbol{u}\boldsymbol{u}) = -\nabla p + \nabla \cdot \boldsymbol{\tau} + \boldsymbol{F}, \tag{1b}$$

$$\partial_t \phi + \nabla \cdot (\boldsymbol{u}\phi) = \nabla \cdot (\boldsymbol{D} \cdot \nabla \phi) + R. \tag{2}$$

In Eq. (1), $\boldsymbol{u} = (u_x, u_y)$ is the velocity in two dimensions (2D), p is the pressure, $\boldsymbol{F} = (F_x, F_y)$ is the external force, and $\boldsymbol{\tau}$ is a second-order tensor representing the shear stress, which can be expressed as

$$\boldsymbol{\tau} = 2\rho_0 \nu \boldsymbol{S}, \tag{3}$$

where ρ_0 is the density of fluid, ν is the kinematic viscosity of fluid, and $\boldsymbol{S}$ is the shear rate defined as

$$\boldsymbol{S} = \tfrac{1}{2}[\nabla \boldsymbol{u} + (\nabla \boldsymbol{u})^T], \tag{4}$$

where the superscript T denotes the transposition operator. In Eq. (2), ϕ is the conserved scalar variable (e.g., concentration, etc.), and $\boldsymbol{D}$ is the symmetric matrix of diffusion coefficients. Finally, R represents the source term, such as chemical reactions.

A. D2Q9-MRT model for incompressible Navier-Stokes equations

Both the NS and the CD equations considered in the present work are confined in 2D. Thereafter, the most popular discrete velocity model, i.e., the D2Q9 (two-dimensional-nine-velocity) model, is used here. The velocity $\boldsymbol{c}_i$ of this model is defined as

$$\boldsymbol{c}_i = \begin{cases} c(0,0), & i = 0, \\ c(\cos[(i-1)\pi/2], \sin[(i-1)\pi/2]), & i = 1,2,3,4, \\ 2c(\cos[(i-5)\pi/2+\pi/4], \sin[(i-5)\pi/2+\pi/4]), & i = 5,6,7,8, \end{cases} \tag{5}$$

where $c = \delta_x/\delta_t$ is the lattice speed, and δ_x and δ_t denote the lattice spacing and the time step, respectively.

The evolution equation of the MRT model for the incompressible NS equations in Eq. (1) can be expressed as follows:

$$f_i(\boldsymbol{x} + \boldsymbol{c}_i\delta_t, t+\delta_t) - f_i(\boldsymbol{x},t) = -(\boldsymbol{M}^{-1}\boldsymbol{\Lambda}\boldsymbol{M})_{ij}\left[f_j(\boldsymbol{x},t) - f_j^{\mathrm{eq}}(\boldsymbol{x},t)\right] + \delta_t\left[\boldsymbol{M}^{-1}\left(\boldsymbol{I} - \tfrac{1}{2}\boldsymbol{\Lambda}\right)\boldsymbol{M}\right]_{ij}\overline{F}_j, \tag{6}$$

where $f_i(\boldsymbol{x},t)$ is the distribution function for particles moving with velocity $\boldsymbol{c}_i$ at position $\boldsymbol{x}$ and time t, $\boldsymbol{\Lambda}$ is the diagonal relaxation matrix in moment space arranged as $\boldsymbol{\Lambda} = (\lambda_0, \ldots, \lambda_8)^T$, in which $\lambda_4 = \lambda_6$ and $\lambda_7 = \lambda_8$, generally, and $\boldsymbol{M}$ is the transformation

matrix defined as

$$\boldsymbol{M} = \begin{bmatrix} 1 & 1 & 1 & 1 & 1 & 1 & 1 & 1 & 1 \\ -4 & -1 & -1 & -1 & -1 & 2 & 2 & 2 & 2 \\ 4 & -2 & -2 & -2 & -2 & 1 & 1 & 1 & 1 \\ 0 & 1 & 0 & -1 & 0 & 1 & -1 & -1 & 1 \\ 0 & -2 & 0 & 2 & 0 & 1 & -1 & -1 & 1 \\ 0 & 0 & 1 & 0 & -1 & 1 & 1 & -1 & -1 \\ 0 & 0 & -2 & 0 & 2 & 1 & 1 & -1 & -1 \\ 0 & 1 & -1 & 1 & -1 & 0 & 0 & 0 & 0 \\ 0 & 0 & 0 & 0 & 0 & 1 & -1 & 1 & -1 \end{bmatrix}. \tag{7}$$

The equilibrium distribution function f_i^{eq} in Eq. (6) plays an important role in the LB method. To recover the incompressible NS equations correctly, here we propose the following formulation on the basis of the LKS model [17] and the He-Luo incompressible model [25], which reads

$$f_i^{\mathrm{eq}} = \omega_i \left\{ \rho + \rho_0 \left[\frac{\boldsymbol{c}_i \cdot \boldsymbol{u}}{c_s^2} + \frac{(\boldsymbol{c}_i \cdot \boldsymbol{u})^2}{2c_s^4} - \frac{\boldsymbol{u}^2}{2c_s^2} + \frac{A\delta_t \boldsymbol{S} : (\boldsymbol{c}_i \boldsymbol{c}_i - c_s^2 \boldsymbol{I})}{2c_s^2} \right] \right\}, \tag{8}$$

where ω_i are the weight coefficients defined as $\omega_0 = 4/9$, $\omega_{1-4} = 1/9$, and $\omega_{5-8} = 1/36$. ρ is a variable related to the pressure as $p = c_s^2 \rho$, while ρ_0 denotes the density of fluid, which is a constant. $c_s = c/\sqrt{3}$ represents the lattice sound speed, and A is a tunable parameter related to the fluid viscosity. The equilibria in the present model are noted to have two advantages over the original ones in Ref. [17]. On the one hand, they can eliminate the compressibility effect; on the other hand, they conserve the mass locally. Finally, to avoid discrete lattice effects in the LB model, the forcing term $\overline{F}_i$ in Eq. (6) is defined as [26]

$$\overline{F}_i = \omega_i \left[\frac{\boldsymbol{c}_i \cdot \boldsymbol{F}}{c_s^2} + \frac{\boldsymbol{u}\boldsymbol{F} : (\boldsymbol{c}_i \boldsymbol{c}_i - c_s^2 \boldsymbol{I})}{c_s^4} \right]. \tag{9}$$

With the transformation matrix $\boldsymbol{M}$, the evolution equation can be rewritten on the basis of Eq. (6) as

$$\begin{aligned} &\boldsymbol{f}(\boldsymbol{x} + \boldsymbol{c}_i \delta_t, t + \delta_t) - \boldsymbol{f}(\boldsymbol{x}, t) \\ &\quad = -\boldsymbol{M}^{-1} \boldsymbol{\Lambda} [\hat{\boldsymbol{f}}(\boldsymbol{x}, t) - \hat{\boldsymbol{f}}^{\mathrm{eq}}(\boldsymbol{x}, t)] + \boldsymbol{M}^{-1} \delta_t \hat{\boldsymbol{F}}, \end{aligned} \tag{10}$$

where $\hat{\boldsymbol{f}}$ are the distribution functions in moment space mapped from those in velocity space $\boldsymbol{f}$ as

$$\hat{\boldsymbol{f}} = \boldsymbol{M} \cdot \boldsymbol{f} = (\rho, e, \varepsilon, j_x, q_x, j_y, q_y, p_{xx}, p_{xy})^T. \tag{11}$$

The equilibrium moments $\hat{\boldsymbol{f}}^{\mathrm{eq}}$ are defined as $\hat{\boldsymbol{f}}^{\mathrm{eq}} = \boldsymbol{M} \cdot \boldsymbol{f}^{\mathrm{eq}}$, which can be written as

$$\begin{aligned} &\hat{f}_0^{\mathrm{eq}} = \rho, \quad \hat{f}_1^{\mathrm{eq}} = -2\rho + \rho_0 [3\boldsymbol{u}^2 + 2A\delta_t (\partial_x u_x + \partial_y u_y)], \\ &\hat{f}_2^{\mathrm{eq}} = \rho - \rho_0 [3\boldsymbol{u}^2 + 2A\delta_t (\partial_x u_x + \partial_y u_y)], \quad \hat{f}_3^{\mathrm{eq}} = \rho_0 u_x, \\ &\hat{f}_4^{\mathrm{eq}} = -\rho_0 u_x, \quad \hat{f}_5^{\mathrm{eq}} = \rho_0 u_y, \quad \hat{f}_6^{\mathrm{eq}} = -\rho_0 u_y, \\ &\hat{f}_7^{\mathrm{eq}} = \rho_0 \left[u_x^2 - u_y^2 + \tfrac{2}{3} A\delta_t (\partial_x u_x - \partial_y u_y) \right], \\ &\hat{f}_8^{\mathrm{eq}} = \rho_0 \left[u_x u_y + \tfrac{1}{3} A\delta_t (\partial_x u_y + \partial_y u_x) \right], \end{aligned} \tag{12}$$

where (see Appendix A for more details)

$$\begin{aligned} \partial_x u_x + \partial_y u_y &= -\frac{\hat{f}_1 - \hat{f}_1^{e(0)} - 3\delta_t \boldsymbol{u} \cdot \boldsymbol{F}}{2(1/\lambda_1 - A)\delta_t}, \\ \partial_x u_x - \partial_y u_y &= -\frac{3\left[\hat{f}_7 - \hat{f}_7^{e(0)} - \delta_t (u_x F_x - u_y F_y)\right]}{2(1/\lambda_7 - A)\delta_t}, \\ \partial_x u_y + \partial_y u_x &= -\frac{3\left[\hat{f}_8 - \hat{f}_8^{e(0)}\right] - 3\delta_t (u_x F_x + u_y F_y)/2}{(1/\lambda_8 - A)\delta_t}, \end{aligned} \tag{13}$$

which can be computed locally with second-order accuracy in the present model (the definitions of $\hat{f}_{1,7,8}^{e(0)}$ are presented in Appendix A). In addition, $\hat{\boldsymbol{F}} = (\boldsymbol{I} - \frac{1}{2}\boldsymbol{\Lambda})\boldsymbol{M}\overline{\boldsymbol{F}}$ in Eq. (10) are the corresponding force moments, which read

$$\begin{aligned} &\hat{F}_0 = 0, \quad \hat{F}_1 = 6\left(1 - \frac{s_1}{2}\right)\boldsymbol{u} \cdot \boldsymbol{F}, \\ &\hat{F}_2 = -6\left(1 - \frac{s_1}{2}\right)\boldsymbol{u} \cdot \boldsymbol{F}, \quad \hat{F}_3 = F_x, \\ &\hat{F}_4 = -\left(1 - \frac{s_4}{2}\right)F_x, \quad \hat{F}_5 = F_y, \\ &\hat{F}_6 = -\left(1 - \frac{s_6}{2}\right)F_y, \\ &\hat{F}_7 = 2\left(1 - \frac{s_7}{2}\right)(u_x F_x - u_y F_y), \\ &\hat{F}_8 = \left(1 - \frac{s_8}{2}\right)(u_x F_y + u_y F_x). \end{aligned} \tag{14}$$

The macroscopic variables can then be obtained from the moments of the distribution functions in velocity space as

$$\rho = \sum_{i=0}^{8} f_i(\boldsymbol{x}, t), \quad \rho_0 \boldsymbol{u} = \sum_{i=0}^{8} \boldsymbol{c}_i f_i(\boldsymbol{x}, t) + \frac{\delta_t}{2}\boldsymbol{F}. \tag{15}$$

Through the Chapman-Enskog analysis, the Navier-Stokes equations (1a) and (1b) can be recovered with (details are presented in Appendix A)

$$\begin{aligned} \nu &= c_s^2\left(\frac{1}{\lambda_7}-\frac{1}{2}-A\right)\delta_t = c_s^2\left(\frac{1}{\lambda_8}-\frac{1}{2}-A\right)\delta_t, \\ \varsigma &= c_s^2\left(\frac{1}{\lambda_1}-\frac{1}{2}-A\right)\delta_t, \end{aligned} \tag{16}$$

where ν and ς are the kinematic and buck viscosities, respectively. Finally, we would like to point out that the velocity gradient term in $f_2^{\rm eq}$ in Eq. (12) has no influence on the recovery of the NS equations (for more details, see Appendix A). We keep this term in the moment so that the model can reduce to the LBGK-B model as all the relaxation rates are taken to be $1/\tau_{\rm SRT}$ ($\tau_{\rm SRT}$ is the relaxation time in the LBGK-B model), which can retain the consistency of these two models.

B. D2Q9-MRT model for the convection-diffusion equation

The evolution equation of the MRT model for the convection-diffusion equation is

$$\begin{aligned} &g_i(\boldsymbol{x}+\boldsymbol{c}_i\delta_t,t+\delta_t)-g_i(\boldsymbol{x},t) \\ &\quad = -(\boldsymbol{M}^{-1}\boldsymbol{\Lambda}'\boldsymbol{M})_{ij}\left[g_j(\boldsymbol{x},t)-g_j^{\rm eq}(\boldsymbol{x},t)\right]+\delta_t\overline{R}_i+\frac{\delta_t^2}{2}\partial_t\overline{R}_i, \end{aligned} \tag{17}$$

where $\boldsymbol{\Lambda}'$ is the diagonal relaxation matrix in moment space, and $\overline{R}_i$ is the source term, which is the same as that used in Ref. [27]. $g_i^{\rm eq}$ is the equilibrium distribution function given as

$$g_i^{\rm eq} = \omega_i\phi\left[1+\frac{\boldsymbol{c}_i\cdot\boldsymbol{u}}{c_s^2}+\frac{(\boldsymbol{c}_i\cdot\boldsymbol{u})^2}{2c_s^4}-\frac{\boldsymbol{u}^2}{2c_s^2}\right]+\omega_i B\delta_t(\boldsymbol{c}_i\cdot\nabla\phi), \tag{18}$$

where B is a tunable parameter related to the diffusion coefficient, and the time derivative term in Eq. (17) can be treated with the finite-difference scheme, e.g., $\partial_t\overline{R}_i = [\overline{R}_i(\boldsymbol{x},t)-\overline{R}_i(\boldsymbol{x},t-\delta_t)]/\delta_t$ [28].

Similarly, the evolution equation in moment space can be written as

$$\begin{aligned} &\boldsymbol{g}(\boldsymbol{x}+\boldsymbol{c}_i\delta_t,t+\delta_t)-\boldsymbol{g}(\boldsymbol{x},t) \\ &\quad = -\boldsymbol{M}^{-1}\boldsymbol{\Lambda}'[\hat{\boldsymbol{g}}(\boldsymbol{x},t)-\hat{\boldsymbol{g}}^{\rm eq}(\boldsymbol{x},t)]+\boldsymbol{M}^{-1}\left[\delta_t\hat{\boldsymbol{R}}+\frac{\delta_t^2}{2}\partial_t\hat{\boldsymbol{R}}\right], \end{aligned} \tag{19}$$

where $\hat{\boldsymbol{R}}$ are the source terms in moment space, which can be expressed as follows:

$$\begin{aligned} &\hat{R}_0 = R, \quad \hat{R}_1 = -2R, \quad R_2 = R, \quad \hat{R}_3 = \left(1-\frac{\lambda_3'}{2}\right)u_xR, \\ &\hat{R}_4 = -\left(1-\frac{\lambda_4'}{2}\right)u_xR, \quad \hat{R}_5 = \left(1-\frac{\lambda_5'}{2}\right)u_yR, \\ &\hat{R}_6 = -\left(1-\frac{\lambda_6'}{2}\right)u_yR, \quad \hat{R}_7 = 0, \quad \hat{R}_8 = 0, \end{aligned} \tag{20}$$

and $\hat{\boldsymbol{g}}^{\rm eq}$ in Eq. (19) are defined as

$$\begin{aligned} &\hat{g}_0^{\rm eq} = \phi, \quad \hat{g}_1^{\rm eq} = \phi(-2+3\boldsymbol{u}^2), \quad \hat{g}_2^{\rm eq} = \phi(1-3\boldsymbol{u}^2), \\ &\hat{g}_3^{\rm eq} = \phi u_x+\tfrac{1}{3}B\delta_t\partial_x\phi, \quad \hat{g}_4^{\rm eq} = -\phi u_x-\tfrac{1}{3}B\delta_t\partial_x\phi, \\ &\hat{g}_5^{\rm eq} = \phi u_y+\tfrac{1}{3}B\delta_t\partial_y\phi, \quad \hat{g}_6^{\rm eq} = -\phi u_y-\tfrac{1}{3}B\delta_t\partial_y\phi, \\ &\hat{g}_7^{\rm eq} = \phi\left(u_x^2-u_y^2\right), \quad \hat{g}_8^{\rm eq} = \phi u_xu_y, \end{aligned} \tag{21}$$

where (see Appendix A for more details)

$$\begin{aligned} \partial_x\phi &= -\frac{3\left[\hat{g}_3-\hat{g}_3^{e(0)}\right]-3\delta_tR_3/2}{(1/\lambda_3'-B)\delta_t}, \\ \partial_y\phi &= -\frac{3\left[\hat{g}_5-\hat{g}_5^{e(0)}\right]-3\delta_tR_5/2}{(1/\lambda_5'-B)\delta_t}, \end{aligned} \tag{22}$$

which can also be computed locally with second-order accuracy here (the definitions of $\hat{g}_{3,5}^{e(0)}$ are presented in Appendix A).

The scalar variable can be obtained by

$$\phi = \sum_{i=0}^{8} g_i. \tag{23}$$

Again through the Chapman-Enskog analysis, Eq. (2) can be recovered from Eq. (19) (details are presented in Appendix A) with $D_{xx} = c_s^2(1/\lambda_3'-1/2-B)\delta_t$ as well as $D_{yy} = c_s^2(1/\lambda_5'-1/2-B)\delta_t$.

To sum up, both Eqs. (1) and (2) can be recovered correctly from the model proposed in this work, and the computations of the fluid viscosity and the diffusion coefficients are different from those in the previous LBGK model [1,9,10] (LBGK-A) and the MRT model [24] (MRT-A). They are determined by not only the corresponding relaxation times, but also the additional tunable parameters A and B. Specifically, as A and B are taken to be 0, the proposed MRT model can reduce to the previous MRT one in Ref. [24]. In addition, as all the relaxation rates in the present model take the value of $1/\tau_{\rm SRT}$, it can reduce to the LBGK-B model in Ref. [16]. Furthermore, the derivatives in Eqs. (12) and (21) can be calculated locally with the corresponding distribution functions in moment space directly (see Appendix A for more details) in the present model, with no need to calculate the second-order moment of the distribution functions as in the LBGK-B model [16]. Hence, the computations of the derivatives in equilibrium functions here are easier than those of the LBGK-B model in Ref. [16].

III. RESULTS AND DISCUSSION

In this section, we will carry out a number of simulations to demonstrate the accuracy and numerical stability of the proposed model. First, a steady Poiseuille flow and a diffusion-reaction problem are simulated to validate the present model. The accuracy of the present model is carefully analyzed on the basis of these two tests. Then, we conduct a comparative study to examine the accuracy of the proposed model of computing the permeability of a specific porous medium. Finally, the viscous displacement problem between two parallel plates is simulated to test the performance of this model.

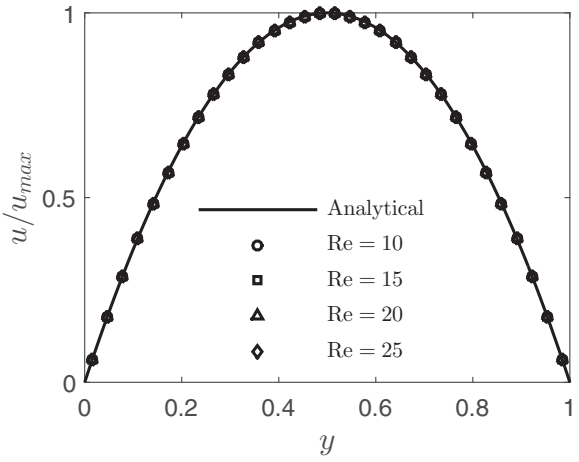

FIG. 1. Velocity profiles at different Reynolds numbers.

A. Accuracy tests

1. Steady Poiseuille flow

The flow between two parallel plates driven by a constant pressure gradient is simulated first. The computational domain is set as $-H/2 \leqslant y \leqslant H/2$ and $0 \leqslant x \leqslant L$, where $H = 1.0$ and $L = 0.5$ are the width and length of the channel, respectively. The initial and boundary conditions are given as follows:

$$\begin{aligned} u(x,y,0) = v(x,y,0) = 0, \quad \rho(x,y,0) = \rho_0, \\ u(x,-H/2,t) = u(x,H/2,t) = v(x,-H/2,t) \\ = v(x,H/2,t) = 0, \\ p(0,y,t) = p_{\text{in}}, \quad p(L,y,t) = p_{\text{out}}, \end{aligned} \tag{24}$$

where ρ_0 is the constant density of fluid, which is set to be 1.0, and p_{in} and p_{out} are the pressure at the inlet and outlet, respectively. The nonslip boundary conditions at the upper and bottom walls are implemented with the halfway bounce-back scheme, and the nonequilibrium extrapolation scheme [29] is used to treat the inlet and outlet boundary conditions. The

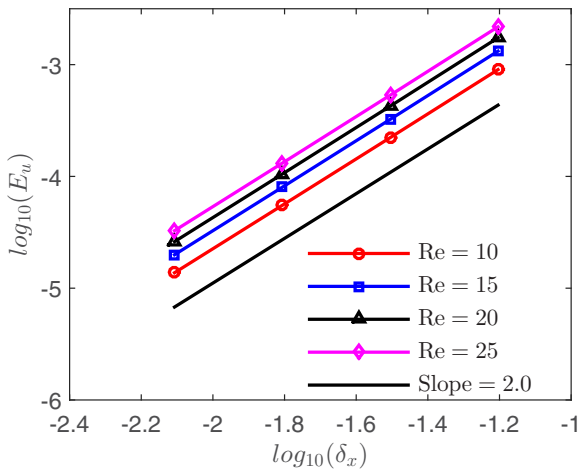

FIG. 2. (Color online) Global relative errors at different mesh sizes and Reynolds numbers.

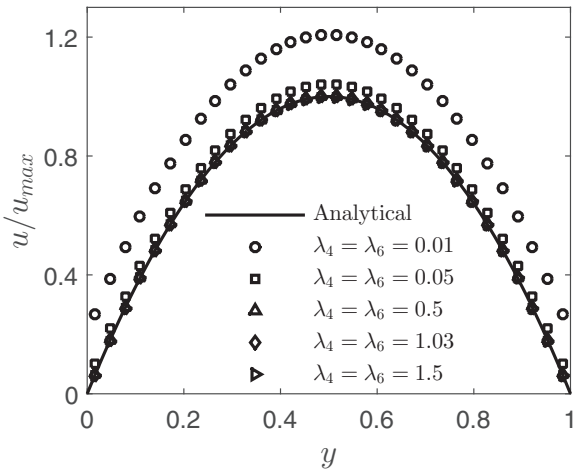

FIG. 3. Velocity profiles at different $\lambda_4(\lambda_6)$.

analytical solution for this problem is

$$u(y) = \frac{G}{\nu}\frac{H^2}{2}\left(\frac{y}{H} - \frac{y^2}{H^2}\right), \tag{25}$$

where ν is the kinematic viscosity of fluid, y is the position in the y direction, and $G = -\partial p/\partial x$ is the pressure gradient.

In our simulations, the dimensionless characteristic parameter Reynolds number (Re) is defined as $\text{Re} = u_{\max}H/\nu$, where $u_{\max} = GH^2/8\nu$ is the maximum velocity obtained from Eq. (25). Four different cases are considered here, i.e., Re = 10, 15, 20, and 25, respectively. The computations are conducted on a 16×32 ($L \times H$) uniform lattice. The convergent criterion for the steady flows is

$$\frac{\sum_{ij} |\boldsymbol{u}(\boldsymbol{x},t + 1000\delta_t) - \boldsymbol{u}(\boldsymbol{x},t)|}{\sum_{ij} |\boldsymbol{u}(\boldsymbol{x},t + 1000\delta_t)|} < 10^{-9}. \tag{26}$$

The choices of the relaxation rates used in the simulations are introduced here. The values of λ_1 and λ_2 are validated to have little influence on the numerical results, so that they are both specified as 1.0. The other relaxation rates are set as $\lambda_0 = \lambda_3 = \lambda_5 = 0$ and $\lambda_7 = \lambda_8 = 1/\tau_\nu = 1.0$ in these cases; the remaining two relaxation rates, λ_4 and λ_6, are chosen to be $\lambda_4 = \lambda_6 = [16(\tau_\nu - A) - 8]/[8(\tau_\nu - A) - 1]$, so that the no-slip boundary condition can be realized exactly (see Appendix B for more details). In addition, the tunable parameter A is fixed as 0.1 in our simulations.

The numerical results of the velocity profiles are illustrated in Fig. 1, and they show good agreement with the analytical solutions at different Reynolds numbers. To further examine the spacial accuracy of the present model, a set of simulations are carried out with four different grid sizes, i.e., 8×16, 16×32, 32×64, and 64×128. The global relative error (GRE) used to measure the accuracy of the model is calculated as

TABLE I. GREs at different values of $\lambda_4(\lambda_6)$.

$\lambda_4(\lambda_6)$	0.01	0.05	0.5	1.03	1.5
E_u	0.2063	3.96×10^{-2}	2.148×10^{-3}	2.223×10^{-4}	6.293×10^{-4}

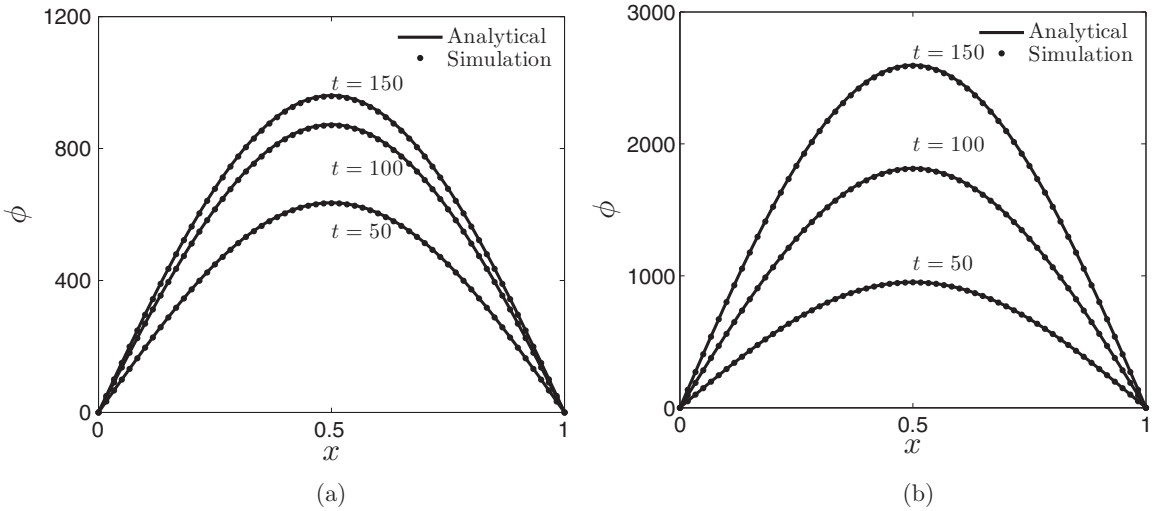

FIG. 4. Concentration profiles at $y = 0.5$ for different diffusion coefficients. (a) $D = 10^{-3}$, (b) $D = 10^{-4}$.

follows:

$$E_u = \sqrt{\frac{\sum_{ij}(\boldsymbol{u} - \boldsymbol{u}^*)^2}{\sum_{ij}(\boldsymbol{u}^*)^2}}, \tag{27}$$

where $\boldsymbol{u}$ and $\boldsymbol{u}^*$ denote the numerical result and the analytical solution, respectively. The relationship between E_u and the lattice spacing δ_x is shown in Fig. 2. The slopes of the fitting lines are 2.0122, 2.0169, 2.0196, and 2.0194 for Re = 10, 15, 20, and 25, respectively. This demonstrates that the present model has second-order accuracy in space.

Furthermore, to investigate the effect of λ_4 and λ_6 on the precise implementation of the no-slip boundary condition, the values of these two parameters are varied, i.e., $\lambda_4 = \lambda_6 = 0.01$, 0.05, 0.5, $[16(\tau_\nu - A) - 8]/[8(\tau_\nu - A) - 1] = 1.03$, and 1.5, while the other relaxation rates are kept unaltered as before. For simplicity, only the case of Re = 10 is simulated on a 16×32 uniform lattice here. As shown in Fig. 3, we can see clearly that the deviations of the optimum choice of λ_4 and λ_6 (1.03) lead to the imprecise implementation of the no-slip boundary condition. In addition, the GREs of the test cases are presented in Table I. It can be concluded that the GRE increases as the value of $\lambda_4(\lambda_6)$ deviates from 1.03.

2. Reaction-diffusion problem

Now we simulate an unsteady diffusion-reaction problem to test the accuracy of the present MRT model for the CDE. Here, we consider a two-dimensional diffusion-reaction system defined in the region $0 \leqslant x, y \leqslant l$, where $l = 1.0$ is the width of the region. The test problem can be described mathematically as follows:

$$\partial_t \phi = D\nabla^2\phi + 2C \sin\frac{\pi x}{l} \sin\frac{\pi y}{l}, \tag{28}$$

where C is a constant taken as 10 in our simulations, and D is the diffusion coefficient. The initial and boundary conditions are

$$\phi(x, y, 0) = 0, \tag{29}$$

$$\phi(0, y, t) = \phi(l, y, t) = \phi(x, 0, t) = \phi(x, l, t) = 0. \tag{30}$$

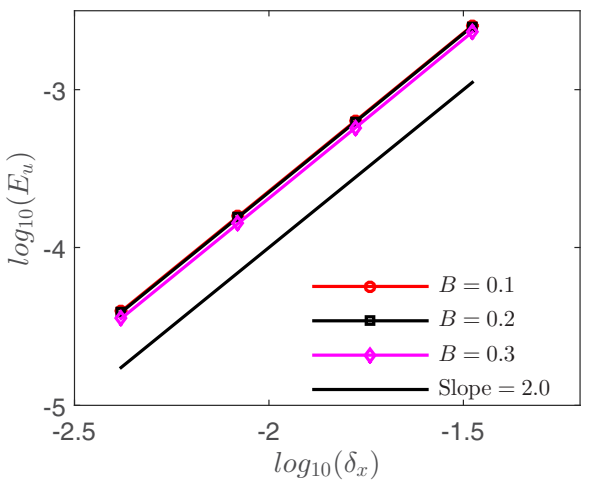

FIG. 5. (Color online) Global relative errors at different mesh sizes.

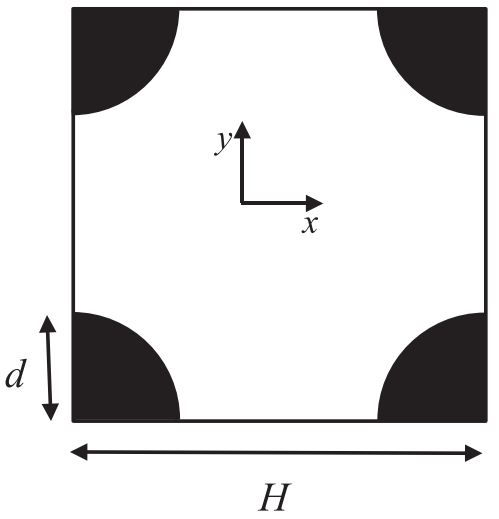

FIG. 6. Circular cylinders in a square array.

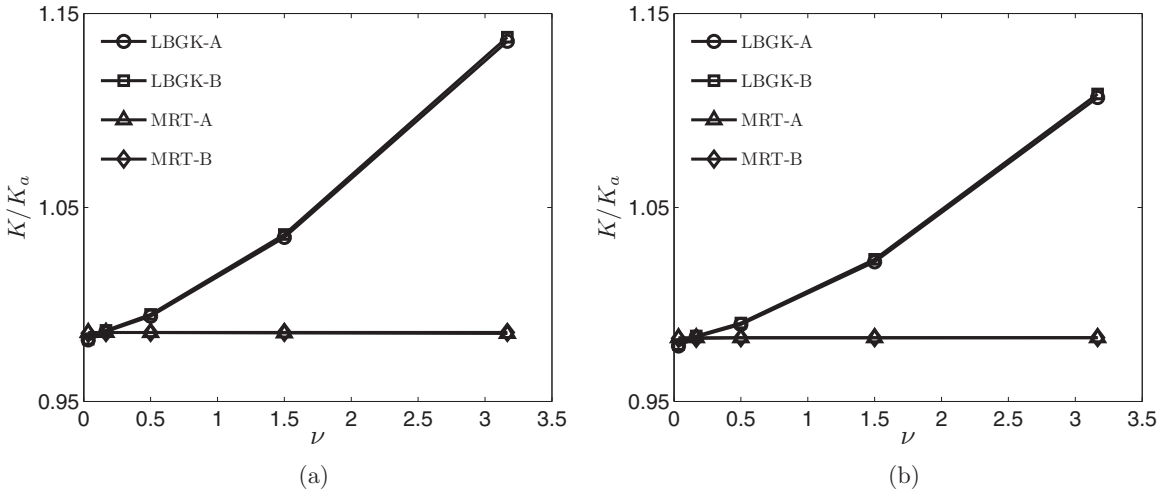

FIG. 7. The permeabilities computed from the four LB models at different viscosities. (a) $d = 41\delta_x$, $\epsilon = 0.967$; (b) $d = 61\delta_x$, $\epsilon = 0.927$.

The nonequilibrium extrapolation scheme [29] is adopted to treat these boundary conditions. The analytical solution for Eq. (28) can be expressed as

$$\phi(x,y,t) = \frac{l^2}{\pi^2 D} C\left[1 - \exp\left(-\frac{2\pi^2 Dt}{l^2}\right)\right] \sin\frac{\pi x}{l} \sin\frac{\pi y}{l}. \tag{31}$$

Our simulations are conducted with a grid of size 60×60, and two different diffusion coefficients are tested, i,e., $D = 10^{-3}$ and 10^{-4}. The numerical results and the analytical solutions are compared at three different times: $t = 50$, 100, and 150 for each D. The relaxation rates are taken as $\lambda'_0 = 1.0$, $\lambda'_1 = \lambda'_2 = 1.1$, $\lambda'_3 = \lambda'_4 = \lambda'_5 = \lambda'_6 = 1/0.9$, and $\lambda'_7 = \lambda'_8 = 1.2$, which are the same as those used in Ref. [30], and the tunable parameter B is determined by the diffusion coefficient. Again, good agreement is observed at different times for each diffusion coefficient, as shown in Fig. 4.

Furthermore, the spacial accuracy of the proposed MRT model is also tested. We conduct the simulations at four grids with sizes of 30×30, 60×60, 120×120, and 240×240, and the relaxation rates are the same as above. The tunable parameter B is taken to be 0.1, 0.2, and 0.3, respectively, to obtain different diffusion coefficients. The global relative error for this problem is defined as

$$E_u = \sqrt{\frac{\sum_{ij}(\phi - \phi^*)^2}{\sum_{ij}(\phi^*)^2}}, \tag{32}$$

where ϕ^* denotes the analytical solution. The relationship between the global error E_u and the lattice spacing δ_x is plotted in Fig. 5, and the slopes of the fitting lines are 2.0037, 2.0067, and 2.0100 for $B = 0.1$, 0.2, and 0.3, respectively. This demonstrates that the proposed MRT model also has second-order accuracy in space.

B. Numerical computation of the permeability of porous media

As reported in the literature [19,31], LB models with a SRT collision operator commonly encounter the defect that the permeability is viscosity-dependent when simulating flow through porous media. However, this deficiency can be

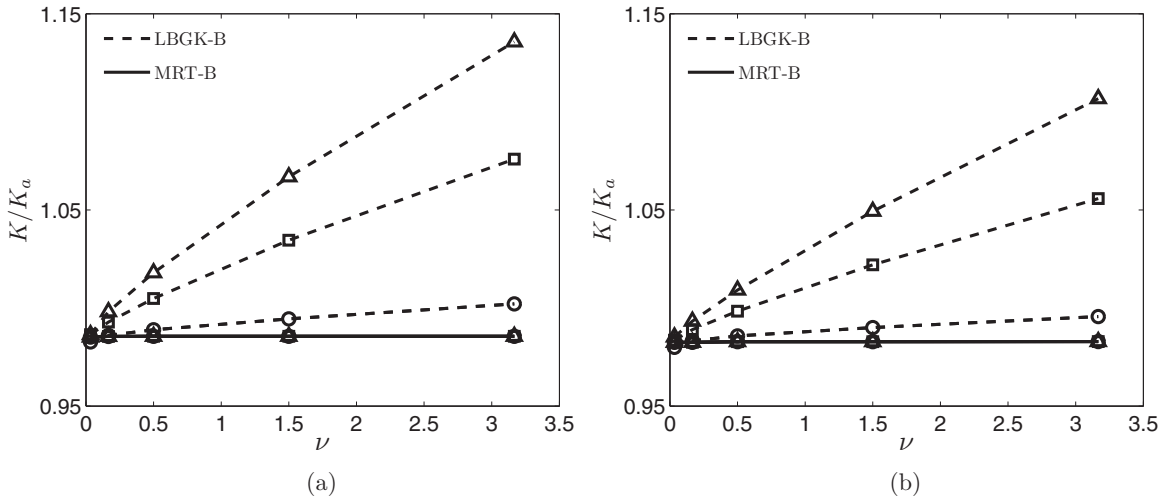

FIG. 8. The permeabilities computed from the LBGK-B and MRT-B models at different viscosities. (a) $d = 41\delta_x$,$\epsilon = 0.967$; (b) $d = 61\delta_x$,$\epsilon = 0.927$. Circle: $\tau = 1.0$, square: $\tau = 5.0$, triangle: $\tau = 10.0$.

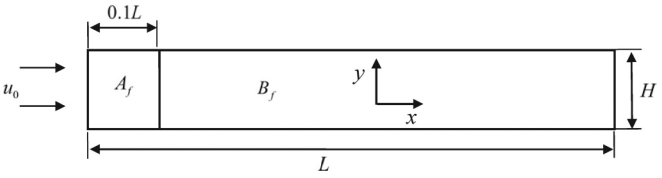

FIG. 9. Geometry of the viscous displacement problem between two parallel plates.

significantly reduced by adopting the MRT model [19,31]. In this subsection, we will test whether the present MRT model can give a correct prediction of the permeability of a porous medium with specific structure. A comparative study is conducted with the LBGK-A model [1,9,10], the LBGK-B model [16], the MRT-A model [24], and the present MRT model (MRT-B). A detailed comparison will be conducted between the LBGK-B model and the present MRT model in particular, since both models employ a modified equilibrium distribution with additional gradient terms. The porous structure is illustrated in Fig. 6, where H is the width of the square array, which is set as 200.0, and d is the diameter of the packed cylinder. The permeability of this porous structure can be expressed analytically as [32]

$$K_a = \frac{d^2}{32\phi}[-\ln\phi - 1.476 + 2\phi - 1.774\phi^2 + 4.706\phi^3], \tag{33}$$

where K_a denotes the analytical permeability of porous media, $\phi = 1.0 - \epsilon$, and $\epsilon = 1.0 - 0.25\pi(d/H)^2$ is the porosity. Meanwhile, the flow through porous media can be described by Darcy's law as

$$u_d = -\frac{K}{\mu}(\partial_x p + G), \tag{34}$$

where u_d is the Darcy velocity defined as the volume-averaged velocity in the flow field, μ is the dynamic viscosity of the fluid,

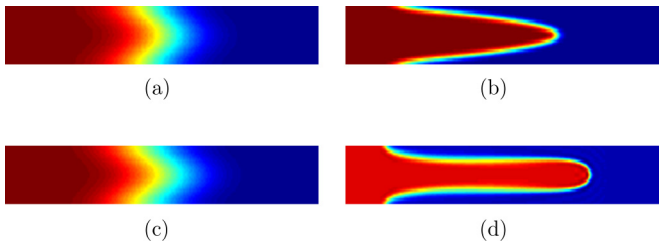

FIG. 11. (Color online) Concentration fields at different M and Pe. (a) $M = 1$, Pe $= 5$; (b) $M = 1$, Pe $= 262$; (c) $M = 100$, Pe $= 5$; and (d) $M = 100$, Pe $= 262$.

p represents the pressure, and G is the external force along the x direction. Thus, the permeability of the porous structure can be evaluated numerically based on Eq. (34) as

$$K = -\frac{\mu u_d}{\partial_x p + G}. \tag{35}$$

The simulations are carried out on an $M \times N = 200 \times 200$ lattice. The flow is driven by the external force G, and the halfway bounce-back rule is used to treat the no-slip boundary condition at the cylinder walls, while the periodic boundary conditions are implemented at the inlet, outlet, bottom, and upper boundaries. The porosity of the specific porous structure is altered by changing the diameter of the packed cylinder. Here we take $d = 41\delta_x$ ($\epsilon \approx 0.967$) and $d = 61\delta_x$ ($\epsilon \approx 0.927$), respectively. The Reynolds number $\mathrm{Re} = u_0 H/\nu$ is taken as 0.1, where ν is the kinematic viscosity, which is related to μ as $\mu = \rho\nu$, and ρ denotes the density of the fluid, which is set as 1.0 in our simulations.

The viscosity dependence of the computed permeability is evaluated with the LBGK-A, LBGK-B, MRT-A, and MRT-B models, respectively. The test kinematic viscosities change from 3.3×10^{-2} to 3.1667. The viscosities are obtained by changing the relaxation times related to the viscosity (τ_ν) from 0.6 to 10.0 in the LBGK-A and MRT-A models, and from 0.8

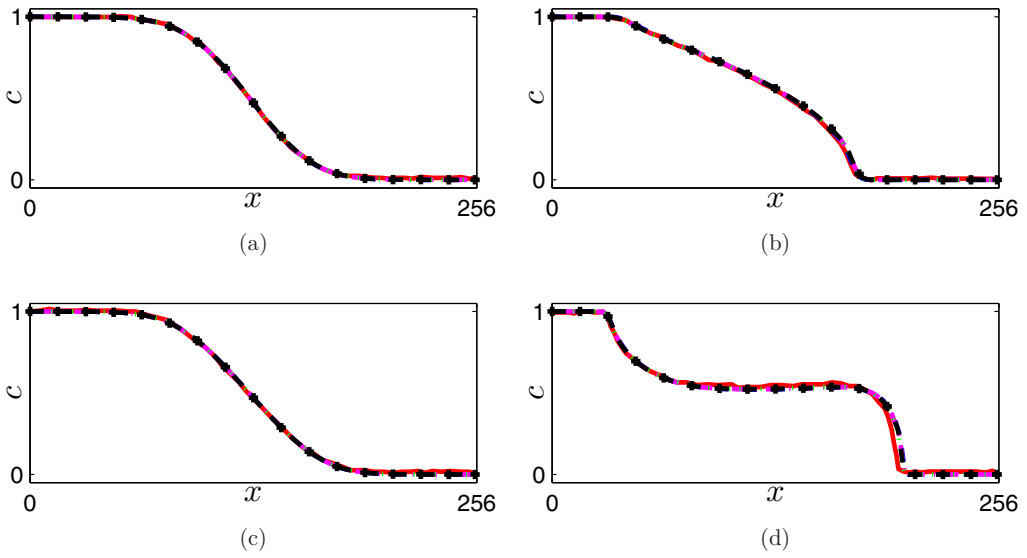

FIG. 10. (Color online) Transverse-averaged concentration profiles at different M and Pe. (a) $M = 1$, Pe $= 5$; (b) $M = 1$, Pe $= 262$; (c) $M = 100$, Pe $= 5$; and (d) $M = 100$, Pe $= 262$. Solid line: results in Ref. [9], dashed line: results of LBGK-A, dot-dashed line: results of LBGK-B, dotted line: results of MRT-A, dashed line with plus: results of MRT-B.

TABLE II. The relaxation times and the tunable parameters related to the kinematic viscosities.

	LBGK-A		LBGK-B		MRT-A		MRT-B	
ν	τ_ν	A	τ_ν	A	τ_ν	A	τ_ν	A
$\nu_A = 0.005$	0.515	0	1.0	0.485	0.515	0	1.0	0.485
$\nu_B = 1.0$	3.5	0	1.0	−2.5	3.5	0	1.0	−2.5
$\nu_B = 2.0$	6.5	0	1.0	−5.5	6.5	0	1.0	−5.5
$\nu_B = 4.0$	12.5	0	1.0	−11.5	11.5	0	1.0	−11.5
$\nu_B = 6.0$	18.5	0	1.0	−17.5	17.5	0	1.0	−17.5

to 10.2 while keeping A as 0.2 in the LBGK-B and MRT-B models to obtain the same viscosity for each case. In addition, the other relaxation rates, i.e., $\lambda_0 = \lambda_3 = \lambda_5 = 0.0$, $\lambda_1 = \lambda_2 = 1.0/\tau_\nu$, and $\lambda_7 = \lambda_8 = 1.0/\tau_\nu$ in MRT-A and MRT-B, are the same, while $\lambda_4 = \lambda_6 = (16\tau_\nu - 8)/(8\tau_\nu - 1)$ in MRT-A and $\lambda_4 = \lambda_6 = [16(\tau_\nu - A) - 8]/[8(\tau_\nu - A) - 1]$ in MRT-B, which can realize the exact no-slip boundary conditions. As shown in Fig. 7, the permeabilities computed by the LBGK-A and LBGK-B models increase by about 15% (from $0.98K_a$ to $1.13K_a$) with the increase of viscosity, which is nonphysical. On the contrary, both the MRT-A and MRT-B models can give nearly a constant permeability.

As described before, the viscosity is altered by changing the value of the corresponding relaxation time in the LBGK-B model and the MRT-B model with a fixed value of A. Considering that the viscosity in each of these two models is determined by the relaxation time and the tunable parameter, here we investigate the robustness of both models by varying the value of the parameter A with a fixed relaxation time τ_ν to obtain different viscosities. Three different values of τ_ν are considered in our simulations ($\tau_\nu = 1.0$, 5.0, and 10.0). The porous structure and the Reynolds number are kept the same as before. The computed permeabilities are shown in Fig. 8. Both Figs. 8(a) and 8(b) indicate that the LBGK-B model cannot overcome the problem of viscosity-dependent permeability even with a fixed relaxation time, while the present MRT model can still provide a satisfactory prediction in each case.

C. Viscous displacement between two parallel plates in two dimensions

In the above subsections, the accuracy of the present model is validated, and the second-order convergence rate in space is

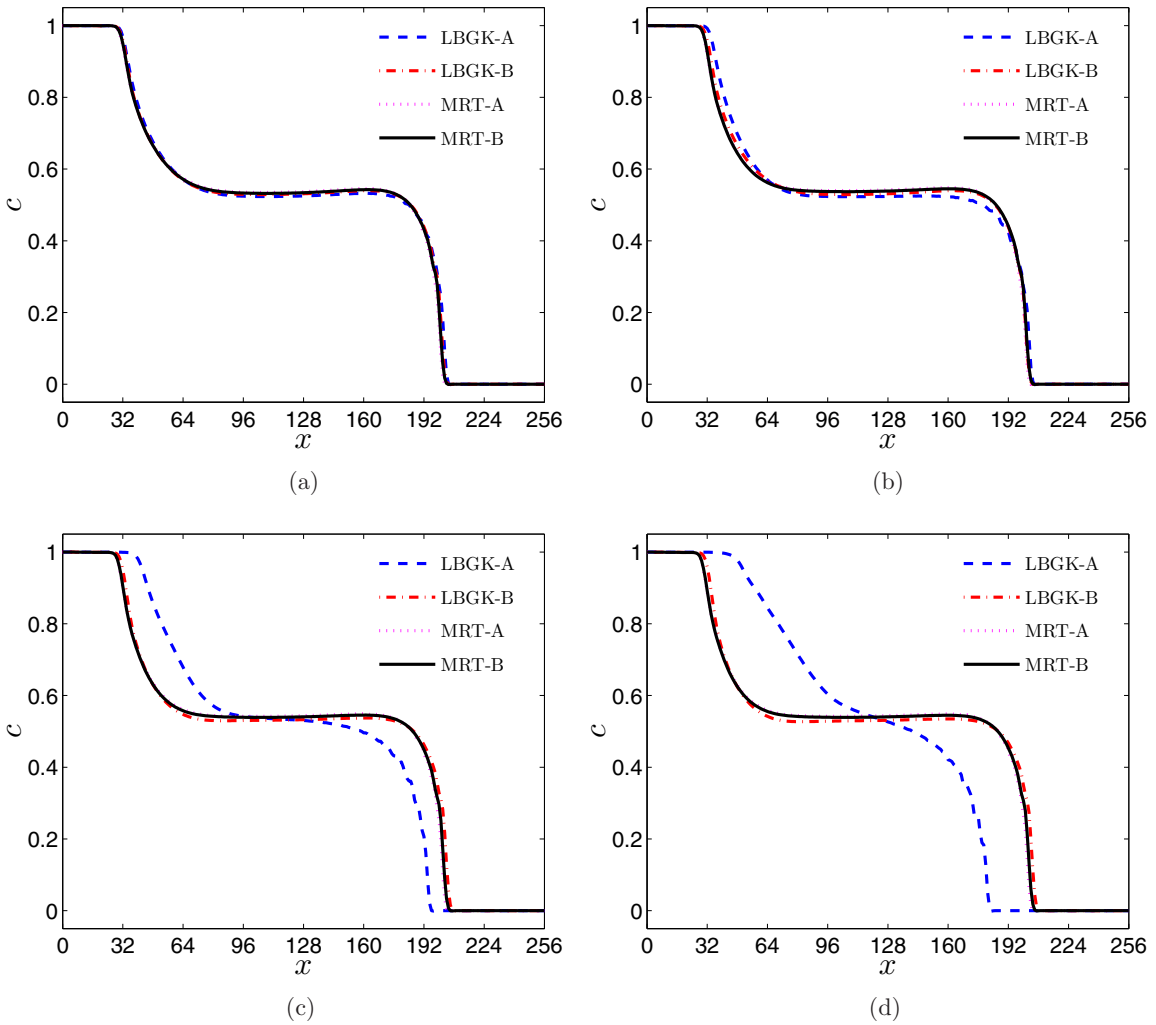

FIG. 12. (Color online) Transverse-averaged concentration profiles of the cases Re = 32 and Pe = 262 at different viscosity ratios. (a) $M = 200$, (b) $M = 400$, (c) $M = 800$, and (d) $M = 1200$.

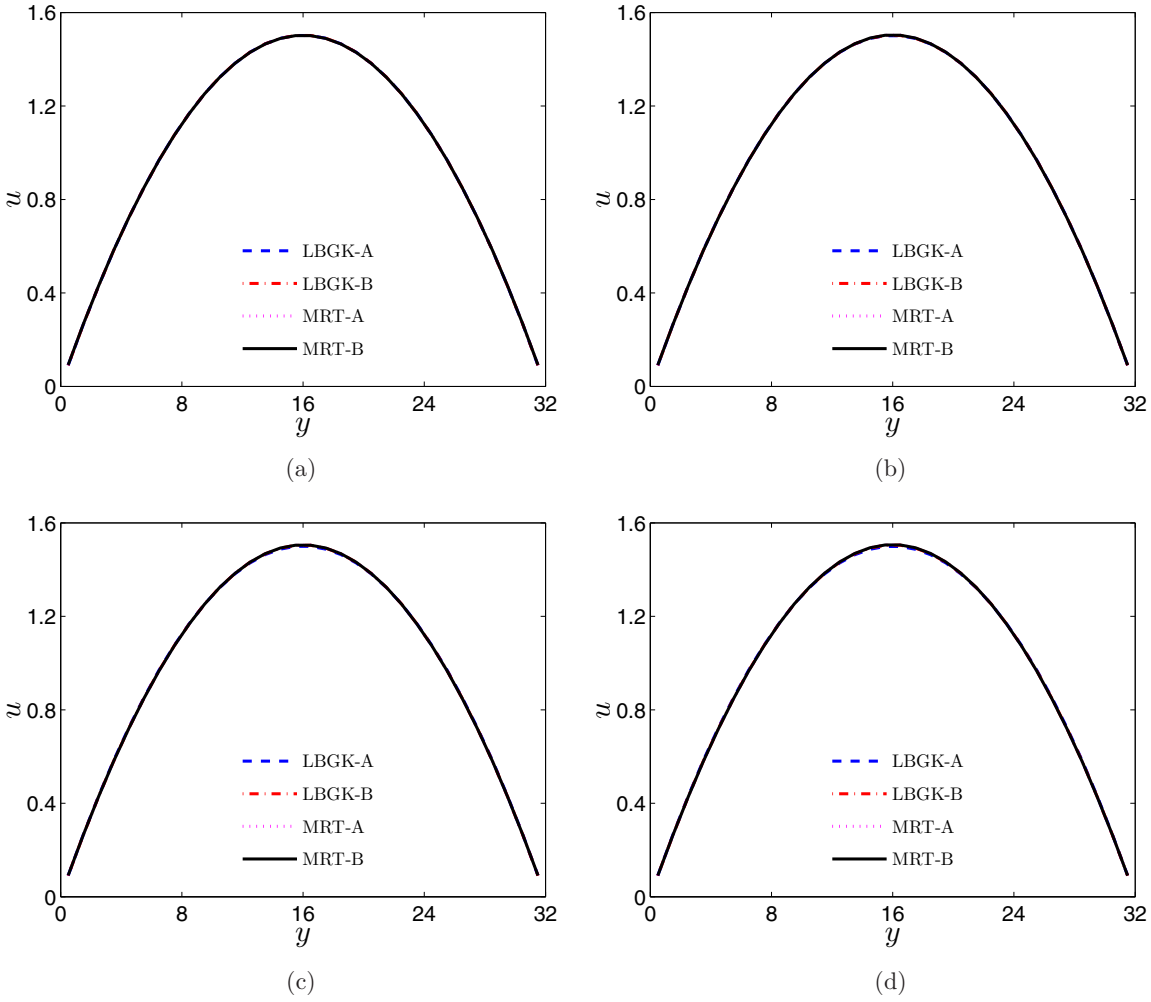

FIG. 13. (Color online) Velocity profiles at the inlet $x = 0$ of the cases Re $= 32$ and Pe $= 262$ at different viscosity ratios. (a) $M = 200$, (b) $M = 400$, (c) $M = 800$, and (d) $M = 1200$.

confirmed. It is also found that this model can give correct predictions of the permeability of porous media. We now examine the capacity of the proposed model for the viscous miscible displacement problem with a large viscosity ratio and a high Péclet number. The test case chosen here is a two-dimensional viscous miscible displacement problem between two parallel plates, as illustrated in Fig. 9. The displacing fluid A_f is injected into the channel with a constant average velocity u_0 (along the x direction) as well as a concentration c_{in} to displace another fluid B_f with concentration $c = 0$. The dynamic viscosity of fluid depends on the local concentration as $\mu = \mu_{A_f} e^{-Rc}$, where R is the log-mobility ratio defined as $R = \ln(M)$, while $M = \mu_{B_f}/\mu_{A_f}$ is the viscosity ratio. This problem was numerically studied by Rakotomalala *et al.* [9] using the LB method.

First, we simulate four cases of the above viscous displacement problem as used in Ref. [9], namely $M = 1$, Pe $= 5$; $M = 1$, Pe $= 262$; $M = 100$, Pe $= 5$; and $M = 100$, Pe $= 262$ to validate our code. All of the following numerical results illustrated in the figures are at 20 000 time steps, which is what Rakotomalala *et al.* did in Ref. [9]. The transverse-averaged concentration profiles obtained from the four LB models are compared with those in Ref. [9]. As shown in Fig. 10, good agreement is observed between the numerical results from the four models and those in Ref. [9]. The concentration fields predicted by the MRT-B model are depicted in Fig. 11, and those from the other three LB models are similar. As shown in Fig. 11, as Pe is small, the diffusion dominates the displacing process, and the mixing region between the two fluids is rather thick. No fingering instability is observed under such cases, even as the viscosity ratio M is as large as 100. Actually, the flow patterns in these two cases are nearly identical. As Pe increases to 262, however, the mixing region becomes much thinner, and the flow pattern depends on the viscosity ratio significantly, which is evident from Figs. 11(b) and 11(d). Specifically, as $M = 100$ and Pe $= 262$, the shape of the displacing fluid evolves toward a well-defined finger, as Rakotomalala *et al.* observed in Ref. [9].

The above numerical results indicate that the four LB models can all provide good predictions of this displacing problem for the cases considered above. However, as noted in Ref. [9], the LBGK-A model works only for a limited range of kinematic viscosities and diffusion coefficients. Those authors pointed out that as the viscosity is large, the corresponding relaxation time will also be large, so that a strong shear near the wall boundaries exists, and the no-slip boundary

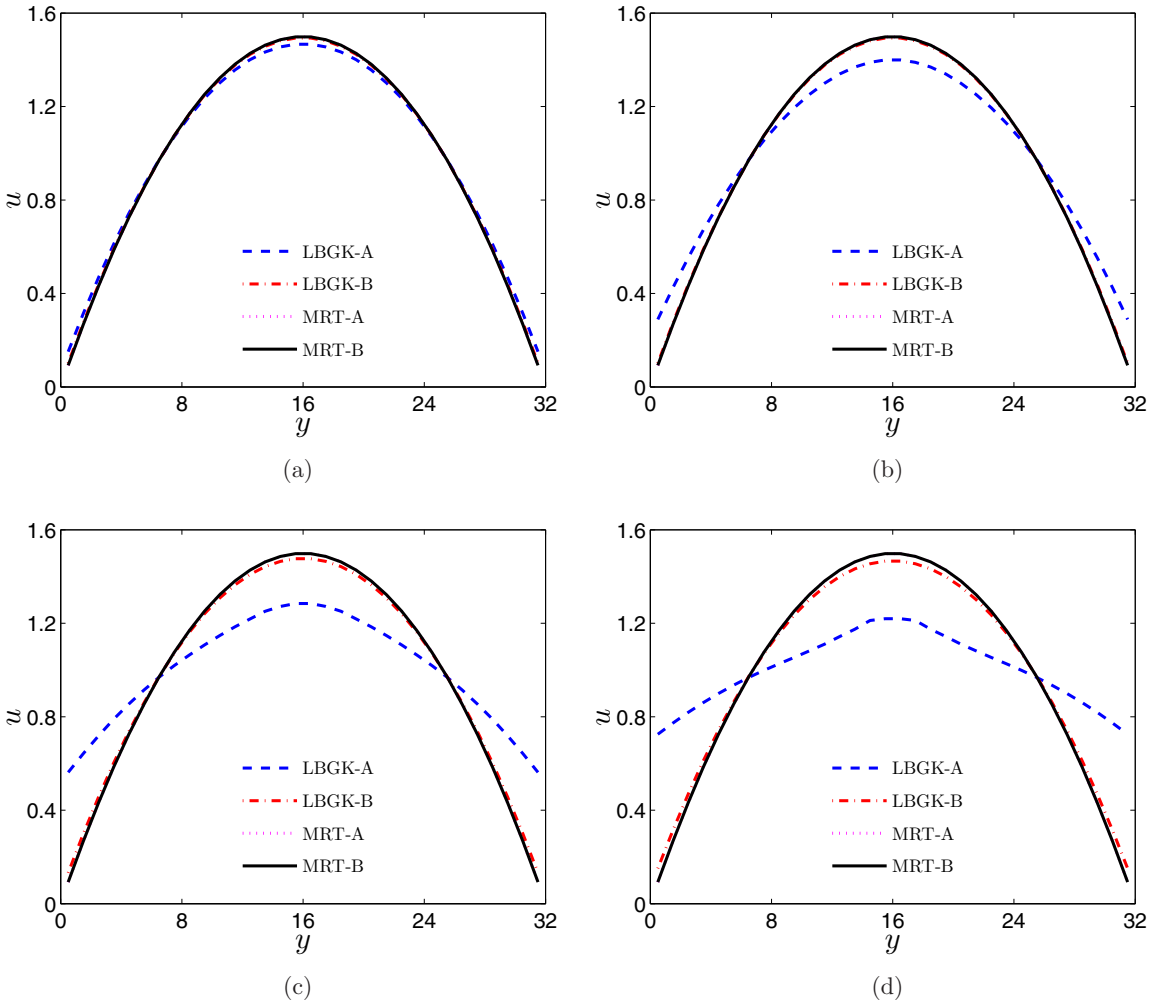

FIG. 14. (Color online) Velocity profiles at the outlet $x = 256$ of the cases Re $= 32$ and Pe $= 262$ at different viscosity ratios. (a) $M = 200$, (b) $M = 400$, (c) $M = 800$, and (d) $M = 1200$.

condition cannot be ensured. On the other hand, a small viscosity and/or diffusion coefficient may lead to numerical instability. These restrictions severely limit the applications of the LBGK-A model in simulating flows with large viscosity ratios and/or high Péclet numbers. The proposed MRT model is expected to overcome these limitations, and now we carry

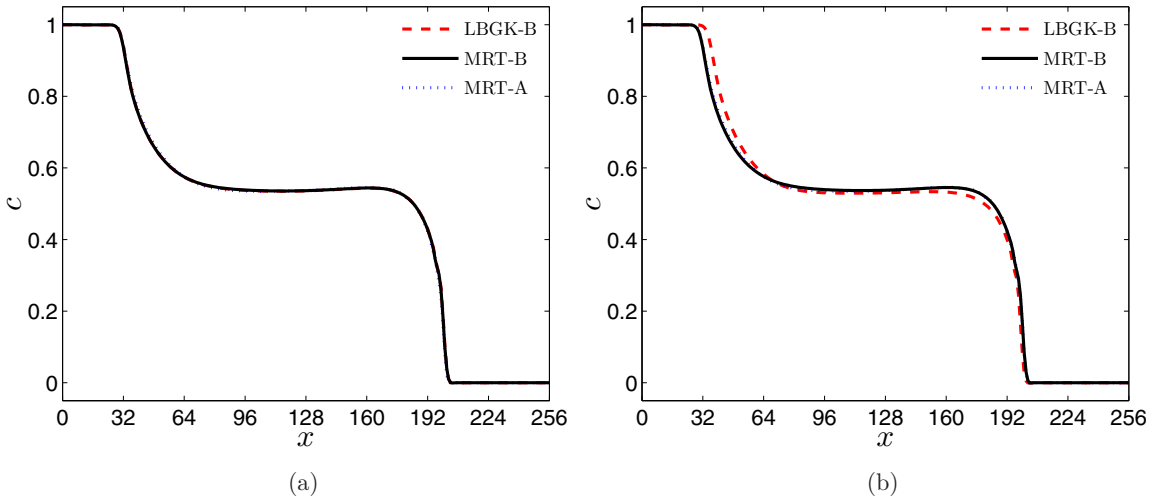

FIG. 15. (Color online) Transverse-averaged concentration profiles of the case $M = 200$, Re $= 32$, and Pe $= 262$ simulated by the LBGK-B and MRT-B models. (a) $\tau_v = 0.6$, (b) $\tau_v = 5.0$.

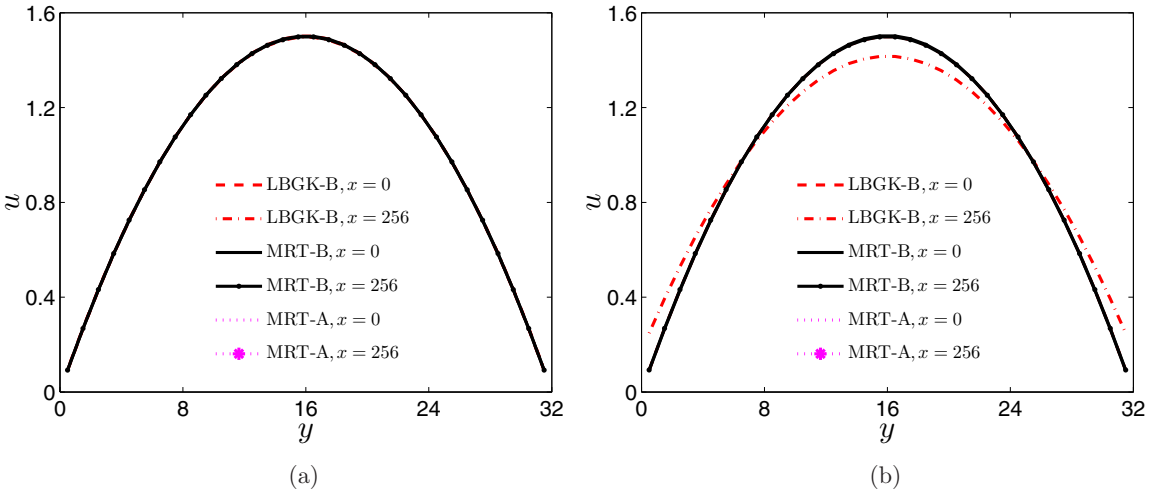

FIG. 16. (Color online) Transverse velocity profiles of the case $M = 200$, Re $= 32$, and Pe $= 262$ simulated by the LBGK-B and MRT-B models. (a) $\tau_v = 0.6$, (b) $\tau_v = 5.0$.

out a comparative study among the four LB models to simulate flow with a large viscosity ratio and/or a high Péclet number.

First we consider a system with large viscosity ratios and a fixed Pe. The Reynolds number Re $= u_0 H/\nu_{A_f}$ is set to be 32, while the average velocity u_0 at the inlet is kept as 0.005 to satisfy the low Mach number assumption, and the Péclet number is fixed at 262 so that the diffusion coefficient is in the proper range. To ensure the stable computations for all four LB models, the kinematic viscosity of fluid A_f is fixed as 0.005, suggesting that the relaxation time τ_v related to the viscosity for fluid A_f in the LBGK-A and MRT-A models is 0.515; on the other hand, τ_v is fixed at 1.0 in the LBGK-B and MRT-B models, as suggested in Ref. [18], and the parameter A is chosen to attain the correct viscosity.

Four viscosity ratios are considered here, i.e., $M = 200$, 400, 800, and 1200. The relaxation times and the tunable parameters related to the kinematic viscosity in the four models are listed in Table II. The other relaxation rates in the MRT-B model are chosen as $\lambda_0 = \lambda_3 = \lambda_5 = 0$, $\lambda_1 = \lambda_2 = \lambda_7 = \lambda_8 = 1.0/\tau_v$, and $\lambda_4 = \lambda_6 = [16(\tau_v - A) - 8]/[8(\tau_v - A) - 1]$, where τ_v is a constant taken as 1.0 as mentioned above; while those of the MRT-A model are $\lambda_0 = \lambda_3 = \lambda_5 = 0$, $\lambda_1 = \lambda_2 = \lambda_7 = \lambda_8 = 1.0/\tau_v$, and $\lambda_4 = \lambda_6 = (16\tau_v - 8)/(8\tau_v - 1)$, where τ_v is determined by the kinematic viscosity directly as $\tau_v = 3\nu/\delta_t + 0.5$. The relaxation rates in the MRT-A and MRT-B models for the convection-diffusion equation of the MRT-A and MRT-B models are set to be $\lambda'_0 = 1.0$, $\lambda'_1 = \lambda'_2 = 1.1$, $\lambda'_3 = \lambda'_4 = \lambda'_5 = \lambda'_6 = 1.0/\tau_c$, and $\lambda'_7 = \lambda'_8 = 1.2$. On the other hand, τ_c is chosen differently in these two models, i.e., it is kept as a constant (1.0) in the present MRT-B model, and the parameter B is adjusted to obtain the diffusion coefficient D needed, while it is directly determined by D in the MRT-A model as $\tau_c = 3D/\delta_t + 0.5$.

The results are illustrated in Figs. 12–14. From Fig. 12, we can see that the transverse-averaged concentration profiles from the MRT-A and MRT-B models are almost the same in the four cases. However, those predicted by the LBGK-A model are quite different, and the difference becomes much more obvious with the increase of M. It is also observed from Fig. 12 that the concentration profiles from the LBGK-B model show little difference as compared with those of the both MRT models, although the disparity increases slightly with increasing M.

The transverse velocity profiles calculated from the four models at the inlet and outlet are shown in Figs. 13 and 14. The velocity in the figures is normalized by u_0. Figure 13 shows that all of the models can predict almost the same velocity profiles at the inlet, but at the outlet the results of the LBGK-A model show significant deviations from other models, especially at a large viscosity ratio (Fig. 14). This can be understood because the relaxation time at the outlet is relatively large in the LBGK-A model as M is large, and the no-slip boundary condition cannot be realized and velocity slip occurs. This is consistent with the previous analysis reported in Ref. [9]. On the other hand, with the inclusion of the additional gradient terms in the equilibrium distribution functions, the relaxation times in the LBGK-B model can be set in a proper range, and so the velocity profiles from the LBGK-B model show no obvious velocity slip at the walls. However, some slight deviations from the results of the two MRT models are still observed, which is due to the inaccurate boundary locations in the SRT models. Overall, the two MRT models can give reasonable velocity predictions for the displacing problem.

We further investigate the robustness of the present model and the LBGK-B model. Without loss of generality, we choose the case with $M = 200$ and Pe $= 262$, and the results from the MRT-A model in Figs. 12–14 are served as a benchmark since the results from the two MRT models shows little difference, which can be observed clearly in Figs. 12–14. The simulation parameters are kept the same as used above, but two different

TABLE III. The relaxation times and the tunable parameters related to the diffusion coefficients.

	MRT-A		MRT-B	
D	τ_c	B	τ_c	B
$D = 4.44 \times 10^{-5}$	0.500 13	0	1.0	0.499 87
$D = 3.56 \times 10^{-5}$	0.500 11	0	1.0	0.499 89

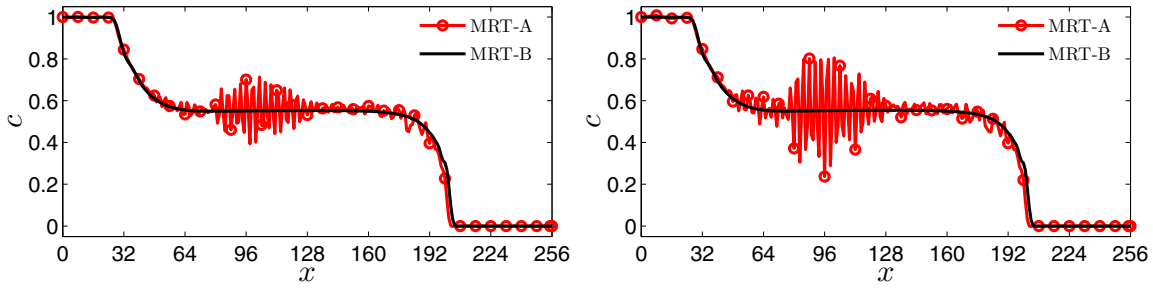

(a) (b)

FIG. 17. (Color online) Transverse-averaged concentration profiles at different Pe as $M = 1200$, Re $= 32$. (a) Pe $= 1200$, (b) Pe $= 1500$.

values of the relaxation time τ_v (0.6 and 5.0) are used to test the dependence of the numerical results (e.g., velocity and concentration profiles) on τ_v. The concentration profiles computed from the two models as well as those from the MRT-A model are shown in Fig. 15. As shown, the concentration profiles from the LBGK-B model show a slight dependence on τ_v, while the results from the present model agree quite well with the benchmark solutions. Moreover, as depicted in Fig. 16, the velocity profiles from the LBGK-B model at the outlet are clearly different from the benchmark one as $\tau_v = 5.0$. On the contrary, the present model can give nearly the same results as the MRT-A model. These facts suggest that the relaxation time in the LBGK-B models must be chosen carefully, but the present model has no such difficulty.

Based on the above results, we can see that both the MRT-A and MRT-B models can be used to simulate miscible fluid flow with a large viscosity ratio but relatively small Péclet numbers. In what follows, these two models are further tested for flows with high Péclet numbers. Two cases will be considered, i.e., Pe $= 1200$ and 1500 as $M = 1200$ and Re $= 32$. The relaxation times and the tunable parameters related to D are listed in Table III, while the other relaxation rates are kept the same as before. The transverse-averaged concentration profiles from the two models are plotted in Fig. 17. It can be observed that some significant nonphysical fluctuations appear for the MRT-A model at high Péclet numbers, and the fluctuation magnitude increases with Pe. However, it is exciting to observe that the concentration profiles from the MRT-B model are very smooth. Furthermore, if the Péclet number increases to 2000, the relaxation time related to the diffusion coefficient in the MRT-A model is rather small such that the model becomes unstable. On the other hand, the proposed MRT-B model can still give a reasonable prediction under the same conditions [Fig. 18(a)]. This suggests that the present model has better numerical stability. Actually, the present model is still stable even as $M = 10^4$ and Pe $= 10^{10}$, and the result is reasonable [Fig. 18(b)].

IV. CONCLUSIONS

An MRT model for the incompressible Navier-Stokes equations and the convection-diffusion equation is proposed on the basis of the LKS model in the present work. The present model can reduce to the standard MRT model as the additional parameters A and B in the equilibrium distribution functions are taken to be 0. Moreover, the LBGK-B model can also be viewed as a special case of the present model if all the relaxation times are identical.

The numerical results of the Poiseuille flow and the diffusion-reaction problem demonstrate that the present model is of second-order accuracy in space. In addition, the present model can predict a viscosity-independent permeability of a porous medium, which cannot be observed in the SRT models. Furthermore, it is found that only the present model can be used to simulate the viscous displacement problem with a large viscous ratio and a high Péclet number among the four models tested in our work. Specifically, we notice that the present model is capable of predicting reasonable results even as the viscosity ratio is as large as 10^4 and the Péclet number is 10^{10}, which demonstrates the superior numerical stability of the present model. Finally, we would like to point out that the proposed model can also be applied to other problems such as

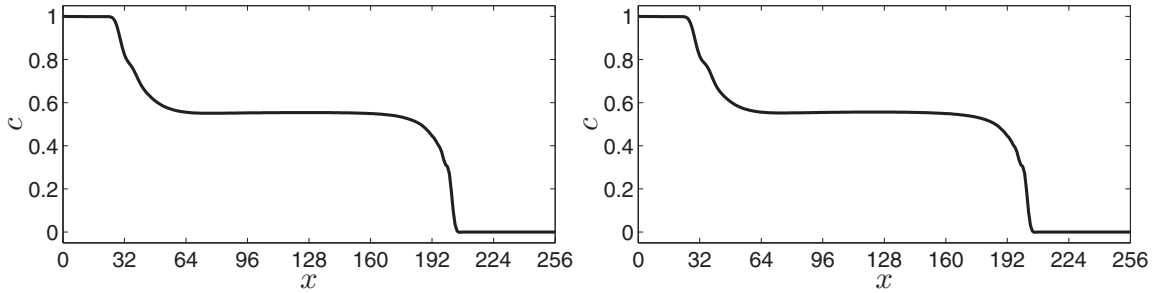

(a) (b)

FIG. 18. Transverse-averaged concentration profiles of flow with a large viscosity ratio as well as high Pe. (a) $M = 1200$, Pe $= 2000$; (b) $M = 10^4$, Pe $= 10^{10}$.

non-Newtonian flow, the advection-diffusion-reaction system with high Péclet numbers, and so on.

ACKNOWLEDGMENTS

The present work is supported by the National Natural Science Foundation of China (No. 51125024) and the Fundamental Research Funds for the Central Universities (HUST: No. 0118120082).

APPENDIX A: CHAPMAN-ENSKOG ANALYSIS OF THE PROPOSED MRT MODEL

In this Appendix, the Navier-Stokes equations and the convection-diffusion equation are derived from the present model through Chapman-Enskog expansion analysis, which introduces the following multiscale expansions:

$$\hat{f}_i = \hat{f}_i^{(0)} + \varepsilon \hat{f}_i^{(1)} + \varepsilon^2 \hat{f}_i^{(2)} + \cdots, \tag{A1}$$

$$\hat{g}_i = \hat{g}_i^{(0)} + \varepsilon \hat{g}_i^{(1)} + \varepsilon^2 \hat{g}_i^{(2)} + \cdots, \tag{A2}$$

$$\partial_t = \varepsilon \partial_{t_0} + \varepsilon^2 \partial_{t_1}, \quad \nabla = \varepsilon \nabla_0, \tag{A3}$$

where ε is a small parameter, and $\hat{f}_i$ and $\hat{g}_i$ are the distribution functions for the density and scalar variables in moment space, respectively. Because the shear rate tensor and the gradient of the scalar variable appear in the equilibrium distribution functions, $\hat{f}_i^{(\mathrm{eq})}$ and $\hat{g}_i^{(\mathrm{eq})}$ can also be expanded into two parts as

$$\hat{f}_i^{(\mathrm{eq})} = \hat{f}_i^{e(0)} + \varepsilon \hat{f}_i^{e(1)}, \tag{A4}$$

$$\hat{g}_i^{(\mathrm{eq})} = \hat{g}_i^{e(0)} + \varepsilon \hat{g}_i^{e(1)}, \tag{A5}$$

which can be expressed in detail as

$$\hat{\boldsymbol{f}}^{e(0)} = \left(\rho, -2\rho + 3\boldsymbol{u}^2, \rho - 3\boldsymbol{u}^2, u_x, -u_x, u_y, -u_y, u_x^2 - u_y^2, u_x u_y\right)^T, \tag{A6}$$

$$\hat{\boldsymbol{f}}^{e(1)} = \left(0, 2A\delta_t(\partial_{0x}u_x + \partial_{0y}u_y), -2A\delta_t(\partial_{0x}u_x + \partial_{0y}u_y), 0, 0, 0, 0, \tfrac{2}{3}A\delta_t(\partial_{0x}u_x - \partial_{0y}u_y), \tfrac{1}{3}A\delta_t(\partial_{0x}u_y + \partial_{0y}u_x)\right)^T, \tag{A7}$$

$$\hat{\boldsymbol{g}}^{e(0)} = \phi\left(1, -2 + 3\boldsymbol{u}^2, 1 - 3\boldsymbol{u}^2, u_x, -u_x, u_y, -u_y, u_x^2 - u_y^2, u_x u_y\right)^T, \tag{A8}$$

$$\hat{\boldsymbol{g}}^{e(1)} = \left(0, 0, 0, \tfrac{1}{3}B\delta_t\partial_{0x}\phi, -\tfrac{1}{3}B\delta_t\partial_{0x}\phi, \tfrac{1}{3}B\delta_t\partial_{0y}\phi, -\tfrac{1}{3}B\delta_t\partial_{0y}\phi, 0, 0\right)^T. \tag{A9}$$

Applying the Taylor expansion to Eqs. (6) and (17), and rewriting them in moment space, we can obtain

$$\boldsymbol{D}\hat{\boldsymbol{f}} + \frac{\delta_t}{2}\boldsymbol{D}^2\hat{\boldsymbol{f}} = -\frac{\boldsymbol{\Lambda}}{\delta_t}[\hat{\boldsymbol{f}} - \hat{\boldsymbol{f}}^{(\mathrm{eq})}], \tag{A10}$$

$$\boldsymbol{D}\hat{\boldsymbol{g}} + \frac{\delta_t}{2}\boldsymbol{D}^2\hat{\boldsymbol{g}} = -\frac{\boldsymbol{\Lambda}'}{\delta_t}[\hat{\boldsymbol{g}} - \hat{\boldsymbol{g}}^{(\mathrm{eq})}], \tag{A11}$$

where $\boldsymbol{D} = \partial_t \boldsymbol{I} + \boldsymbol{C}_{\boldsymbol{\alpha}}\partial_{\boldsymbol{\alpha}}$, in which $\boldsymbol{I}$ is the unit matrix and $\boldsymbol{C}_{\boldsymbol{\alpha}}$ is the discrete velocity matrix.

Substituting Eqs. (A1) and (A4) into (A10), we can obtain the following equations in different orders of ε:

$$\varepsilon^0 : \hat{\boldsymbol{f}}^{(0)} = \hat{\boldsymbol{f}}^{e(0)}, \tag{A12a}$$

$$\varepsilon^1 : \boldsymbol{D}_0\hat{\boldsymbol{f}}^{(0)} = -\frac{\boldsymbol{\Lambda}}{\delta_t}[\hat{\boldsymbol{f}}^{(1)} - \hat{\boldsymbol{f}}^{e(1)}] + \boldsymbol{F}^{(1)}, \tag{A12b}$$

$$\varepsilon^2 : \partial_{t1}\hat{\boldsymbol{f}}^{(0)} + \boldsymbol{D}_0\hat{\boldsymbol{f}}^{(1)} + \frac{\delta_t}{2}\boldsymbol{D}_0^2\hat{\boldsymbol{f}}^{(0)} = -\frac{\boldsymbol{\Lambda}}{\delta_t}\hat{\boldsymbol{f}}^{(2)}. \tag{A12c}$$

$$\varepsilon^0 : \hat{\boldsymbol{g}}^{(0)} = \hat{\boldsymbol{g}}^{e(0)}, \tag{A12d}$$

$$\varepsilon^1 : \boldsymbol{D}_0\hat{\boldsymbol{g}}^{(0)} = -\frac{\boldsymbol{\Lambda}'}{\delta_t}[\hat{\boldsymbol{g}}^{(1)} - \hat{\boldsymbol{g}}^{e(1)}] + \hat{\boldsymbol{R}}^{(1)}, \tag{A12e}$$

$$\varepsilon^2 : \partial_{t1}\hat{\boldsymbol{g}}^{(0)} + \boldsymbol{D}_0\hat{\boldsymbol{g}}^{(1)} + \frac{\delta_t}{2}\boldsymbol{D}_0^2\hat{\boldsymbol{g}}^{(0)} = -\frac{\boldsymbol{\Lambda}'}{\delta_t}\hat{\boldsymbol{g}}^{(2)}, \tag{A12f}$$

where $\boldsymbol{D}_0 = \partial_{t_0}\boldsymbol{I} + \boldsymbol{C}_\alpha\partial_{0\alpha}$. Substituting Eq. (A12b) into the left-hand side of Eq. (A12c), we can obtain

$$\partial_{t1}\hat{\boldsymbol{f}}^{(0)} + \boldsymbol{D}_0\left(\boldsymbol{I} - \frac{\boldsymbol{\Lambda}}{2}\right)\hat{\boldsymbol{f}}^{(1)} + \boldsymbol{D}_0\left[\frac{\boldsymbol{\Lambda}}{2}\hat{\boldsymbol{f}}^{e(1)}\right] + \frac{\delta_t}{2}\boldsymbol{D}_0\boldsymbol{F}^{(1)} = -\frac{\boldsymbol{\Lambda}}{\delta_t}\hat{\boldsymbol{f}}^{(2)}. \tag{A13}$$

In addition, from Eq. (A12a) we can derive

$$\rho^{(k)} = j_x^{(k)} = j_y^{(k)} = 0, \quad k > 0. \tag{A14}$$

Then on the t_0 time scale, Eq. (A12b) can be rewritten as follows:

$$\partial_{0x}(u_x)+\partial_{0y}(u_y)=0, \tag{A15a}$$

$$\begin{aligned}\partial_{t_0}[(-2\rho+3\boldsymbol{u}^2)] &= -\frac{\lambda_1}{\delta_t}\left[e^{(1)}-\hat{f}_1^{e(1)}\right]+6\left(1-\frac{\lambda_1}{2}\right)\boldsymbol{u}\cdot\boldsymbol{F}^{(1)}\\ &= -\frac{\lambda_1}{\delta_t}[e^{(1)}-2A\delta_t(\partial_{0x}u_x+\partial_{0y}u_y)]+6\left(1-\frac{\lambda_1}{2}\right)\boldsymbol{u}\cdot\boldsymbol{F}^{(1)},\end{aligned} \tag{A15b}$$

$$\partial_{t0}(u_x)+\partial_{0x}\left(p+u_x^2\right)+\partial_{0y}(u_xu_y)=F_x^{(1)}, \tag{A15c}$$

$$\partial_{t0}(u_y)+\partial_{0x}(u_xu_y)+\partial_{0y}\left(p+u_y^2\right)=F_y^{(1)}, \tag{A15d}$$

$$\begin{aligned}\partial_{t0}\left[\left(u_x^2-u_y^2\right)\right]+\partial_{0x}\left(\frac{2}{3}u_x\right)+\partial_{0y}\left(\frac{-2}{3}u_y\right) &= -\frac{\lambda_7}{\delta_t}\left[p_{xx}^{(1)}-\hat{f}_7^{e(1)}\right]+2\left(1-\frac{\lambda_7}{2}\right)\left[u_xF_x^{(1)}-u_yF_y^{(1)}\right]\\ &= -\frac{\lambda_7}{\delta_t}\left[p_{xx}^{(1)}-\frac{2}{3}A\delta_t(\partial_{0x}u_x-\partial_{0y}u_y)\right]+2\left(1-\frac{\lambda_7}{2}\right)\left(u_xF_x^{(1)}-u_yF_y^{(1)}\right),\end{aligned} \tag{A15e}$$

$$\begin{aligned}\partial_{t0}(u_xu_y)+\partial_{0x}\left(\frac{1}{3}u_y\right)+\partial_{0y}\left(\frac{1}{3}u_x\right) &= -\frac{\lambda_8}{\delta_t}\left[p_{xy}^{(1)}-mf_8^{e(1)}\right]+\left(1-\frac{\lambda_8}{2}\right)\left[u_xF_{ay}^{(1)}+u_yF_{ax}^{(1)}\right]\\ &= -\frac{\lambda_8}{\delta_t}\left[p_{xy}^{(1)}-\frac{1}{3}A\delta_t(\partial_{0x}u_y+\partial_{0y}u_x)\right]+\left(1-\frac{\lambda_8}{2}\right)\left[u_xF_{ay}^{(1)}+u_yF_{ax}^{(1)}\right].\end{aligned} \tag{A15f}$$

Similarly, Eq. (A12c) can be rewritten on the t_1 time scale as

$$\partial_{t1}\rho=0, \tag{A16a}$$

$$\begin{aligned}&\partial_{t1}(\rho u_x)+\frac{1}{6}\left(1-\frac{\lambda_1}{2}\right)\partial_{0x}e^{(1)}+\left(1-\frac{\lambda_7}{2}\right)\left[\frac{1}{2}\partial_{0x}p_{xx}^{(1)}+\partial_{0y}p_{xy}^{1}\right]+\partial_{0x}\left[\frac{\lambda_1}{2}\left(\frac{1}{6}m_2^{e(1)}\right)+\frac{\lambda_7}{2}\left(\frac{1}{2}m_8^{e(1)}\right)\right]\\ &+\partial_{0y}\left(\frac{\lambda_7}{2}m_9^{e(1)}\right)+\frac{\delta_t}{2}\left\{\partial_{0x}\left[\left(1-\frac{\lambda_1}{2}\right)\boldsymbol{u}\cdot\boldsymbol{F}^{(1)}+\left(1-\frac{\lambda_7}{2}\right)\left(u_xF_x^{(1)}-u_yF_y^{(1)}\right)\right]+\partial_{0y}\left[\left(1-\frac{\lambda_7}{2}\right)\left(u_xF_{ay}^{(1)}+u_yF_{ax}^{(1)}\right)\right]\right\}=0,\end{aligned} \tag{A16b}$$

$$\begin{aligned}&\partial_{t1}(\rho u_y)+\left(1-\frac{\lambda_8}{2}\right)\left[\partial_{0x}p_{xy}^{1}-\frac{1}{2}\partial_{0y}p_{xx}^{(1)}\right]+\frac{1}{6}\left(1-\frac{\lambda_1}{2}\right)\partial_{0y}e^{(1)}+\partial_{0x}\left(\frac{\lambda_8}{2}m_9^{e(1)}\right)+\partial_{0y}\left[\frac{\lambda_1}{2}\left(\frac{1}{6}m_2^{e(1)}\right)+\frac{\lambda_8}{2}\left(\frac{-1}{2}m_8^{e(1)}\right)\right]\\ &+\frac{\delta_t}{2}\left\{\partial_{0x}\left[\left(1-\frac{\lambda_8}{2}\right)\left(u_xF_y^{(1)}+u_yF_x^{(1)}\right)\right]+\partial_{0y}\left[\left(1-\frac{\lambda_1}{2}\right)\boldsymbol{u}\cdot\boldsymbol{F}^{(1)}-\left(1-\frac{\lambda_8}{2}\right)\left(u_xF_x^{(1)}-u_yF_y^{(1)}\right)\right]\right\}=0.\end{aligned} \tag{A16c}$$

Moreover, we can obtain the following expression under the low Mach number assumption that

$$\partial_{t_0}(u_iu_j)=-u_j\partial_{0i}p-u_i\partial_{0j}p+u_iF_j^{(1)}+u_jF_i^{(1)}. \tag{A17}$$

With the help of Eq. (A17), Eqs. (A15b), (A15e), and (A15f) can be expressed as

$$-\frac{\lambda_1e^{(1)}}{\delta_t}=2(1-A\lambda_1)(\partial_{0x}u_x+\partial_{0y}u_y)+3\lambda_1\boldsymbol{u}\cdot\boldsymbol{F}^{(1)}, \tag{A18a}$$

$$-\frac{\lambda_7p_{xx}^{(1)}}{\delta_t}=\frac{2}{3}(1-A\lambda_7)(\partial_{0x}u_x-\partial_{0y}u_y)+\lambda_7\left(u_xF_x^{(1)}-u_yF_y^{(1)}\right), \tag{A18b}$$

$$-\frac{\lambda_8p_{xy}^{(1)}}{\delta_t}=\frac{1}{3}(1-A\lambda_8)(\partial_{0x}u_y-\partial_{0y}u_x)+\frac{\lambda_8}{2}\left(u_xF_y^{(1)}+u_yF_x^{(1)}\right). \tag{A18c}$$

Considering that $\varepsilon e^{(1)}=\hat{f}_1-\hat{f}_1^{e(0)}$, the derivative term $(\partial_xu_x+\partial_yu_y)$ in $\hat{f}_1^{e(1)}$ can be obtained as

$$\partial_xu_x+\partial_yu_y=-\frac{\hat{f}_1-\hat{f}_1^{e(0)}-3\delta_t\boldsymbol{u}\cdot\boldsymbol{F}}{2(1/\lambda_1-A)\delta_t}. \tag{A19}$$

Meanwhile, the derivative terms in $\hat{f}_7^{e(1)}$ and $\hat{f}_8^{e(1)}$ can also be obtained in a similar way.

Substituting Eq. (A18) into Eqs. (A16b) and (A16c), we can obtain that

$$\partial_{t1}(u_x) = \partial_{0x}\left[c_s^2\left(\frac{1}{\lambda_1}-\frac{1}{2}-A\right)\delta_t(\partial_{0x}u_x+\partial_{0y}u_y)\right]+\partial_{0x}\left[c_s^2\left(\frac{1}{\lambda_7}-\frac{1}{2}-A\right)\delta_t(\partial_{0x}u_x-\partial_{0y}u_y)\right]$$
$$+\partial_{0y}\left[c_s^2\left(\frac{1}{\lambda_8}-\frac{1}{2}-A\right)\delta_t(\partial_{0x}u_y+\partial_{0y}u_x)\right], \tag{A20a}$$

$$\partial_{t1}(u_y) = \partial_{0x}\left[c_s^2\left(\frac{1}{\lambda_8}-\frac{1}{2}-A\right)\delta_t(\partial_{0x}u_y+\partial_{0y}u_x)\right]+\partial_{0y}\left[c_s^2\left(\frac{1}{\lambda_7}-\frac{1}{2}-A\right)\delta_t(\partial_{0y}u_y-\partial_{0x}u_x)\right]$$
$$+\partial_{0y}\left[c_s^2\left(\frac{1}{\lambda_1}-\frac{1}{2}-A\right)\delta_t(\partial_{0x}u_x+\partial_{0y}u_y)\right]. \tag{A20b}$$

Coupling the equations on the t_0 and t_1 scale, the macroscopic equations (1) can be obtained.

Similarly, with the help of Eq. (A12e), we can rewrite Eq. (A12f) as

$$\boldsymbol{D}\hat{\boldsymbol{g}}+\frac{\delta_t}{2}\boldsymbol{D}^2\hat{\boldsymbol{g}}=-\frac{\boldsymbol{\Lambda}'}{\delta_t}(\hat{\boldsymbol{g}}-\hat{\boldsymbol{g}}^{(\mathrm{eq})})+\hat{\boldsymbol{R}}+\frac{\delta_t}{2}\partial_t\hat{\boldsymbol{R}}. \tag{A21}$$

We can also derive equations on the t_0 and t_1 time scale as follows:

$$\partial_{t_0}\phi+\partial_{0x}(\phi u_x)+\partial_{0y}(\phi u_y)=R^1, \tag{A22a}$$

$$\partial_{t1}\phi=\partial_{0x}\left[c_s^2\left(\frac{1}{\lambda_3'}-\frac{1}{2}-B\right)\delta_t\partial_{0x}\phi\right]+\partial_{0y}\left[c_s^2\left(\frac{1}{\lambda_5'}-\frac{1}{2}-B\right)\delta_t\partial_{0y}\phi\right]. \tag{A22b}$$

Combining the equations on t_0 and t_1 scale, we can then obtain Eq. (2). Similarly, the derivatives in Eq. (21) can be calculated locally as follows:

$$\partial_x\phi=-\frac{3\left[\hat{g}_3-\hat{g}_3^{e(0)}\right]-3\delta_t R_3/2}{(1/\lambda_3'-B)\delta_t}, \tag{A23a}$$

$$\partial_y\phi=-\frac{3\left[\hat{g}_5-\hat{g}_5^{e(0)}\right]-3\delta_t R_5/2}{(1/\lambda_5'-B)\delta_t}. \tag{A23b}$$

APPENDIX B: ANALYSIS OF THE CHOICE OF λ_4 (OR λ_6) FOR THE NO-SLIP BOUNDARY CONDITION

Numbers of previous studies have indicated that the relaxation rate λ_4 has a significant influence on the precise implementation of the no-slip boundary condition. Therefore, the choice of λ_4 in the present MRT model will be carefully analyzed in this section.

As shown in Fig. 19, we consider a steady incompressible Poiseuille flow driven by a constant force $\boldsymbol{F}=\rho(F_x,0)$ for simplicity, in which we assume that

$$\frac{\partial\psi}{\partial t}=0,\quad \rho=\mathrm{const},\quad u_y=0,\quad \frac{\partial\psi}{\partial x}=0, \tag{B1}$$

where ψ is an arbitrary flow variable.

To begin with, we can obtain the following expressions based on the relationship between $\boldsymbol{f}$ and $\hat{\boldsymbol{f}}$ at the node $i=1$:

$$f_1^1-f_3^1=\tfrac{1}{3}j_x^1-\tfrac{1}{3}q_x^1, \tag{B2}$$

$$f_5^1-f_6^1=\tfrac{1}{3}j_x^1+\tfrac{1}{6}q_x^1+\tfrac{1}{2}p_{xy}^1, \tag{B3}$$

$$f_8^1-f_7^1=\tfrac{1}{3}j_x^1+\tfrac{1}{6}q_x^1-\tfrac{1}{2}p_{xy}^1, \tag{B4}$$

from which we can obtain

$$j_x^1=u_x-\frac{\delta_t}{2}F_x. \tag{B5}$$

Next, the postcollision distribution functions can also be expressed in a similar way as follows:

$$f_1'^1-f_3'^1=\tfrac{1}{3}j_x'^1-\tfrac{1}{3}q_x'^1, \tag{B6}$$

$$f_5'^1-f_6'^1=\tfrac{1}{3}j_x'^1+\tfrac{1}{6}q_x'^1+\tfrac{1}{2}p_{xy}'^1, \tag{B7}$$

$$f_8'^1-f_7'^1=\tfrac{1}{3}j_x'^1+\tfrac{1}{6}q_x'^1-\tfrac{1}{2}p_{xy}'^1, \tag{B8}$$

where ψ' $(\psi=f,q,p)$ are the postcollision distribution functions. Meanwhile, the postcollision distribution functions

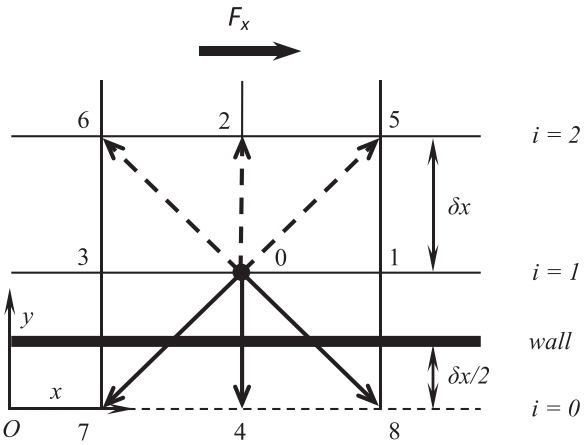

FIG. 19. Schematic of force driven flow and the lattice arrangement.

in moment space in Eqs. (B6)–(B8) can be obtained from Eq. (10), and they can be expressed as

$$j_x'^1 = (1-\lambda_3)j_x^1 + \lambda_3 u_x + \left(1-\frac{\lambda_3}{2}\right)F_x\delta_t, \tag{B9}$$

$$q_x'^1 = (1-\lambda_4)q_x^1 - \lambda_4 u_x - \left(1-\frac{\lambda_4}{2}\right)F_x\delta_t, \tag{B10}$$

$$p_{xy}'^1 = (1-\lambda_8)p_{xy}^1 + \frac{\lambda_8}{3}A\delta_t(\partial_x u_y + \partial_y u_x), \tag{B11}$$

where Eq. (B11) can be rewritten as follows with the aid of Eq. (13):

$$p_{xy}'^1 = \left[1-\lambda_8 - \frac{A\lambda_8}{(1/\lambda_8 - A)}\right]p_{xy}. \tag{B12}$$

Then, substituting Eq. (B5) into Eq. (B9), we can obtain that

$$j_x'^1 = u_x + \frac{F_x\delta_t}{2}. \tag{B13}$$

In addition, we can get the following relationship from the unidirectional property of the flow:

$$f_1^1 - f_3^1 = f_1'^1 - f_3'^1. \tag{B14}$$

Combining Eqs. (B2), (B5), (B6), (B10), and (B13), we can obtain

$$q_x^1 = -u_x - \left(\frac{2}{\lambda_4} - \frac{1}{2}\right)F_x\delta_t, \tag{B15}$$

$$q_x'^1 = -u_x - \left(\frac{2}{\lambda_4} - \frac{3}{2}\right)F_x\delta_t. \tag{B16}$$

It should be noted that the relationships between the distribution functions at $i = 1$ and 2 are

$$f_5^2 - f_6^2 = f_5'^1 - f_6'^1, \quad f_8^1 - f_7^1 = f_8'^2 - f_7'^2. \tag{B17}$$

Similarly, substituting Eqs. (B3), (B4), (B7), and (B8) into (B17), we can obtain the expression of p_{xy}^1 as follows:

$$p_{xy}^1 = \frac{(1/\lambda_8 - A)[(2/\lambda_8 - 2A - 1)(u_1 - u_2) - 3F_x\delta_t]}{3(2/\lambda_8 - 2A - 1)}, \tag{B18}$$

and then $p_{xy}'^1$ can also be obtained with the help of Eq. (B12). Furthermore, we can also obtain the following relationship as the bounce-back scheme is adopted:

$$f_5^1 - f_6^1 = f_7'^1 - f_8'^1. \tag{B19}$$

With these results at hand, the relationship between u_2 and u_1 can now be obtained as follows:

$$u_2 = 3u_1 + \left[2 - 4\tau_q - \frac{3}{2(\tau_\nu - A - 0.5)}\right]F_x\delta_t, \tag{B20}$$

where $\tau_q = 1.0/\lambda_4 = 1.0/\lambda_6$ and $\tau_\nu = 1.0/\lambda_7 = 1.0/\lambda_8$.

As for the steady Poiseuille flow considered here, the velocity can be written as

$$u_i = 4u_c\frac{y_i}{L}\left(1-\frac{y_i}{L}\right) + u_s, \quad i = 1,2, \tag{B21}$$

where $y_i = (i-0.5)\delta_x$, $u_c = F_x L^2/8\nu$, and u_s represents the slip velocity resulting from the bounce-back boundary condition. Substituting Eq. (B21) into Eq. (B20), we can obtain the dimensionless slip velocity,

$$U_s = \frac{u_s}{u_c} = -\frac{16(\tau_q - 0.5)(\tau_\nu - A - 0.5) - 3}{3}\Delta^2, \tag{B22}$$

where $\Delta = \delta_x/L$, and U_s can be zero if τ_q is chosen as $[8(\tau_\nu - A) - 1]/[16(\tau_\nu - A) - 8]$. Thus, the corresponding relaxation rates λ_4 and λ_6 in the present model to satisfy the no-slip boundary condition are

$$\lambda_4 = \lambda_6 = \frac{16(\tau_\nu - A) - 8}{8(\tau_\nu - A) - 1}. \tag{B23}$$

[1] R. Holme and D. H. Rothman, J. Stat. Phys. **68**, 409 (1992).
[2] N. Rakotomalala, D. Salin, and P. Watzky, Phys. Fluids **8**, 3200 (1996).
[3] E. Lajeunesse, J. Martin, N. Rakotomalala, D. Salin, and Y. C. Yortsos, J. Fluid Mech. **398**, 299 (1999).
[4] M. N. Islam and J. Azaiez, Int. J. Numer. Meth. Fluids **47**, 161 (2005).
[5] S. G. Ayodele, F. Varnik, and D. Raabe, Phys. Rev. E **80**, 016304 (2009).
[6] S. G. Ayodele, F. Varnik, and D. Raabe, Phys. Rev. E **83**, 016702 (2011).
[7] S. G. Ayodele, D. Raabe, and F. Varnik, Commun. Comput. Phys. **13**, 741 (2013).
[8] S. G. Ayodele, D. Raabe, and F. Varnik, Phys. Rev. E **91**, 022913 (2015).
[9] N. Rakotomalala, D. Salin, and P. Watzky, J. Fluid Mech. **338**, 277 (1997).
[10] M. Leconte, J. Martin, N. Rakotomalala, and D. Salin, Phys. Rev. Lett. **90**, 128302 (2003).
[11] A. M. Tartakovsky and P. Meakin, J. Comput. Phys. **207**, 610 (2005).
[12] A. M. Tartakovsky and P. S. Neuman, Geophys. Res. Lett. **35**, L21401 (2008).
[13] J. D. Stering and S. Chen, J. Comput. Phys. **123**, 196 (1996).
[14] S. Gabbanelli, G. Drazer, and J. Koplik, Phys. Rev. E **72**, 046312 (2005).
[15] X. Q. Xiang, Z. H. Wang, and B. C. Shi, Commun. Nonlin. Sci. Numer. Simul. **17**, 2415 (2012).
[16] X. G. Yang, B. C. Shi, and Z. H. Chai, Phys. Rev. E **90**, 013309 (2014).
[17] T. Inamuro, Philos. Trans. R. Soc. London, Ser. A **360**, 477 (2002).
[18] L. Wang, J. C. Mi, X. H. Meng, and Z. L. Guo, Commun. Comput. Phys. **17**, 908 (2015).
[19] C. Pan, L. S. Luo, and C. T. Miller, Comput. Fluids **35**, 898 (2006).
[20] P. Lallemand and L. S. Luo, Phys. Rev. E **61**, 6546 (2000).

[21] D. d'Humières, I. Ginzburg, M. Krafczyk, P. Lallemand, and L. S. Luo, Philos. Trans. R. Soc. London, Ser. A **360**, 437 (2002).
[22] M. Krafczyk, J. Tölke, and L. S. Luo, Int. J. Mod. Phys. B **17**, 33 (2003).
[23] N. K. Premnath and J. Abraham, J. Comput. Phys. **224**, 539 (2007).
[24] T. Zhang, Ph.D. thesis, Huazhong University of Science and Technology, 2012.
[25] X. He and L. S. Luo, J. Stat. Phys. **88**, 927 (1997).
[26] Z. L. Guo and C. G. Zheng, Int. J. Comput. Fluid Dyn. **22**, 465 (2008).
[27] B. C. Shi and Z. L. Guo, Phys. Rev. E **79**, 016701 (2009).
[28] B. Deng, B. C. Shi, and G. C. Wang, Chin. Phys. Lett. **22**, 267 (2005).
[29] Z. L. Guo, C. G. Zheng, and B. C. Shi, Chin. Phys. **11**, 366 (2002).
[30] R. Z. Huang and H. Y. Wu, J. Comput. Phys. **274**, 50 (2014).
[31] Z. H. Chai, B. C. Shi, J. H. Lu, and Z. L. Guo, Comput. Fluids **39**, 2069 (2010).
[32] A. S. Sangani and A. Acrivos, Int. J. Multiphase Flow **8**, 193 (1982).